



Subsurface CO₂ dynamics in a temperate karst system reveal complex seasonal and spatial variations

5 Sarah Rowan^{1,2}, Marc Luetscher³, Thomas Laemmel^{1,2}, Anna Harrison⁴, Sönke Szidat^{1,2}, Franziska A
Lechleitner^{1,2}

¹ Department of Chemistry, Biochemistry, and Pharmaceutical Sciences, University of Bern, 3012, Bern, Switzerland.

² Oeschger Centre for Climate Change Research (OCCR), University of Bern, 3012, Bern, Switzerland

³ Swiss Institute of Speleology and Karst Studies, 2300, La Chaux-de-Fonds, Switzerland.

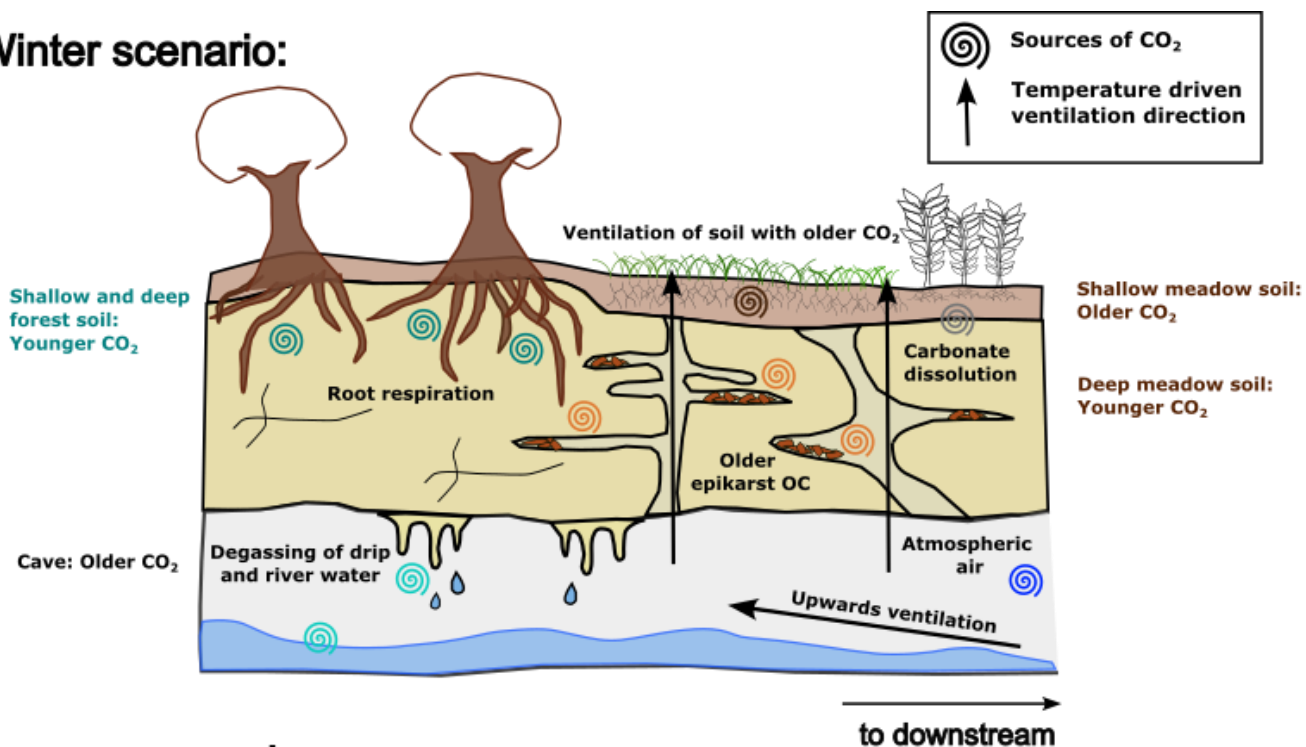
10 ⁴ Institute of Geological Sciences, University of Bern, 3012, Bern, Switzerland.

Correspondence to: Sarah Rowan (sarahrowan96gmail.com)

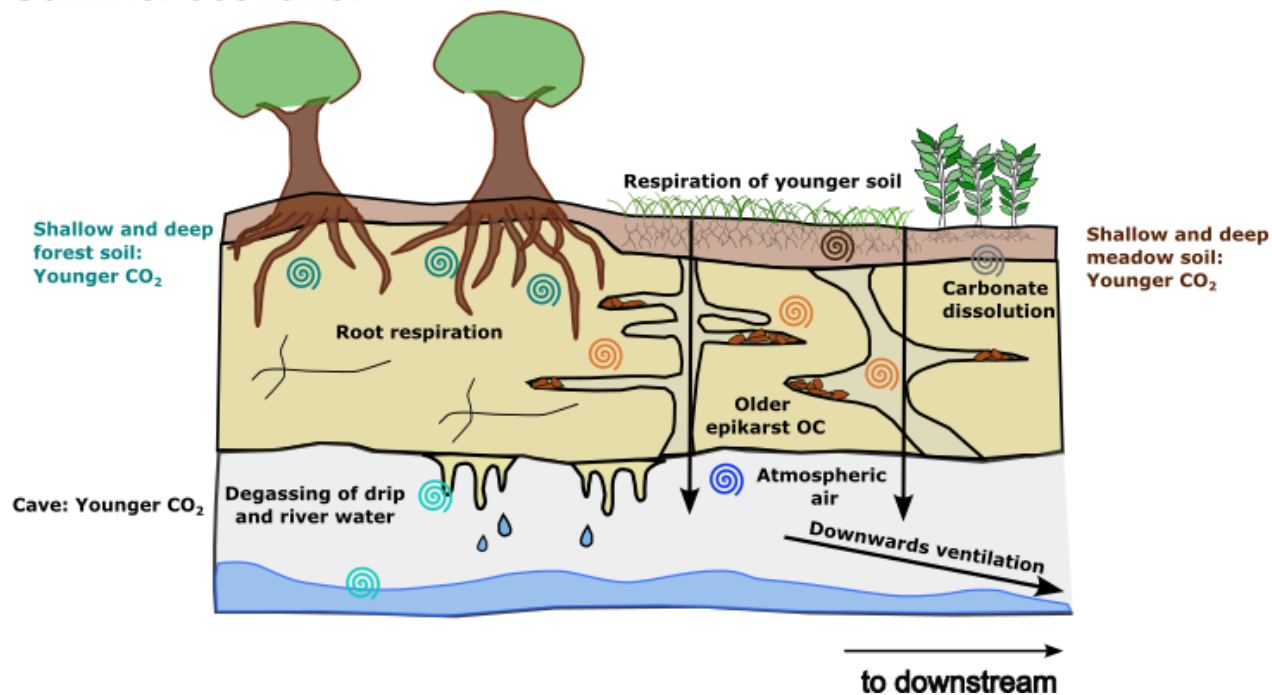
Abstract. Understanding the carbon cycle of the terrestrial Critical Zone, extending from the tree canopy to the aquifer, is crucial for accurate quantification of its total carbon storage and for modelling terrestrial carbon stock responses to climate change. Caves and their catchments offer a natural framework to sample and analyse carbon in unsaturated zone reservoirs across various spatial and temporal scales. In this study, we analyse the concentration, stable carbon isotopic ratio ($\delta^{13}\text{C}$), and radiocarbon (^{14}C) compositions of CO_2 from atmosphere, boreholes (0.5 to 5 m depth), and cave sampled every two months over two years at Milandre cave in northern Switzerland. High concentrations of up to 35'000 ppmV CO_2 are measured in the boreholes. The $\delta^{13}\text{C}$ values of CO_2 in the boreholes reflect the $\delta^{13}\text{C}$ of C3 plants (~ -26 ‰) which dominate the catchment ecosystem. Shallow meadow boreholes host older CO_2 in winter and modern CO_2 in summer, while forest ecosystems consistently export modern CO_2 ($F^{14}\text{C} = \sim 1$) to the unsaturated zone. Cave CO_2 concentrations exceed atmospheric levels and are diluted by temperature-driven seasonal ventilation. Keeling plot intercepts indicate that the cave CO_2 , which mixes with atmospheric CO_2 , is younger in summer ($F^{14}\text{C} = 0.94$) and older in winter ($F^{14}\text{C} = 0.88$), with a $\delta^{13}\text{C}$ consistent with the C3 plant dominated catchment. Mixing models utilising drip water dissolved inorganic carbon ^{14}C suggest that varying carbonate dissolution and degassing dynamics do not explain the $F^{14}\text{C}$ variation and $\delta^{13}\text{C}$ stability of the mixing endmember. Rather, contributions from deeper aged carbon in the epikarst are likely. This study provides valuable insights into CO_2 source dynamics and cycling within karstic Critical Zones, highlighting the impact of seasonal variations and ecological factors on downward carbon export from terrestrial ecosystems.



Winter scenario:



Summer scenario:





1 Introduction

Within the context of current and future changing climate, investigations into the response of Critical Zone carbon pools to rising temperatures and changing hydroclimatic conditions are crucial (Brantley et al, 2007). Recent studies have specifically highlighted the unsaturated zone as a potentially important but poorly constrained reservoir of gaseous CO₂ (Mattey et al., 2016; Noronha et al., 2015; Keller, 2019; Stewart et al., 2022). Estimates suggest that between 2 to 53 PgC could be present in the form of CO₂ in the unsaturated zone globally (Baldini et al., 2018). This carbon is particularly vulnerable to changes in the water table level, whereby rises may easily result in the rapid release of CO₂ into the atmosphere (Baldini et al., 2018). Despite its importance, comprehensive assessments integrating spatial and temporal variability of shallow subsurface CO₂ remain scarce.

40

Understanding unsaturated zone CO₂ dynamics is complicated by the different sources of carbon contributing to the subsurface reservoir. The CO₂ present in the unsaturated zone is often referred to as ground air and was first defined as CO₂ produced by microbial oxidation of organic material which was transported from the surface (Atkinson, 1977). However, ground air can also refer more generally to high CO₂ concentrations in the subsurface, without linking its presence to a particular source. Early evidence for the presence of a ground air reservoir was the observation of high CO₂ concentrations found in deep cave passages with poor connection to the catchment surface, suggesting an endogenous source of CO₂ (McDonough et al., 2016). The age profile of this high concentration CO₂ reservoir, however, varies by site, suggesting significant variability in its source and processing. Exclusively aged CO₂ reservoirs have been reported (Breecker et al., 2012; Noronha et al., 2015; Mattey et al., 2016; Bergel et al., 2017), as well as modern subsurface CO₂ pools, likely derived from ecosystem respiration of recently fixed carbon (Campeau et al., 2019; Tune et al., 2020). Consequently, the primary sources of subsurface CO₂ generally considered are 1) the outside atmosphere (Kukuljan et al., 2021), 2) catchment soil and vegetation respiration (Breecker et al., 2012; Li et al., 2024), 3) microbial respiration in the unsaturated zone (Mattey et al., 2016; Ravn et al., 2020), 4) carbon dissolved from the carbonate bedrock (Milanolo & Gabrovšek, 2015), and 6) volcanic and metamorphic hydrothermal input (Chiodini et al., 2008; Girault et al., 2018).

55

Carbon isotope analysis of CO₂ can be used to differentiate the contributing sources to the subsurface gas mixture. Specifically, the δ¹³C of CO₂ in the unsaturated zone can provide information about the influence of biological fractionation by overlying catchment vegetation and respiration by microorganisms, and the influence of carbonate dissolution and subsequent degassing (Breecker et al., 2017, McDonough et al., 2016). In addition, due to the contrast between the ¹⁴C content of biospheric carbon, which ranges from bomb peak enriched to >10⁴000 years old, and carbonate rock which is typically radiocarbon dead, ¹⁴C measurement of subsurface CO₂ can provide information for both source apportionment and carbon turnover rates in the terrestrial subsurface (Noronha et al., 2015).

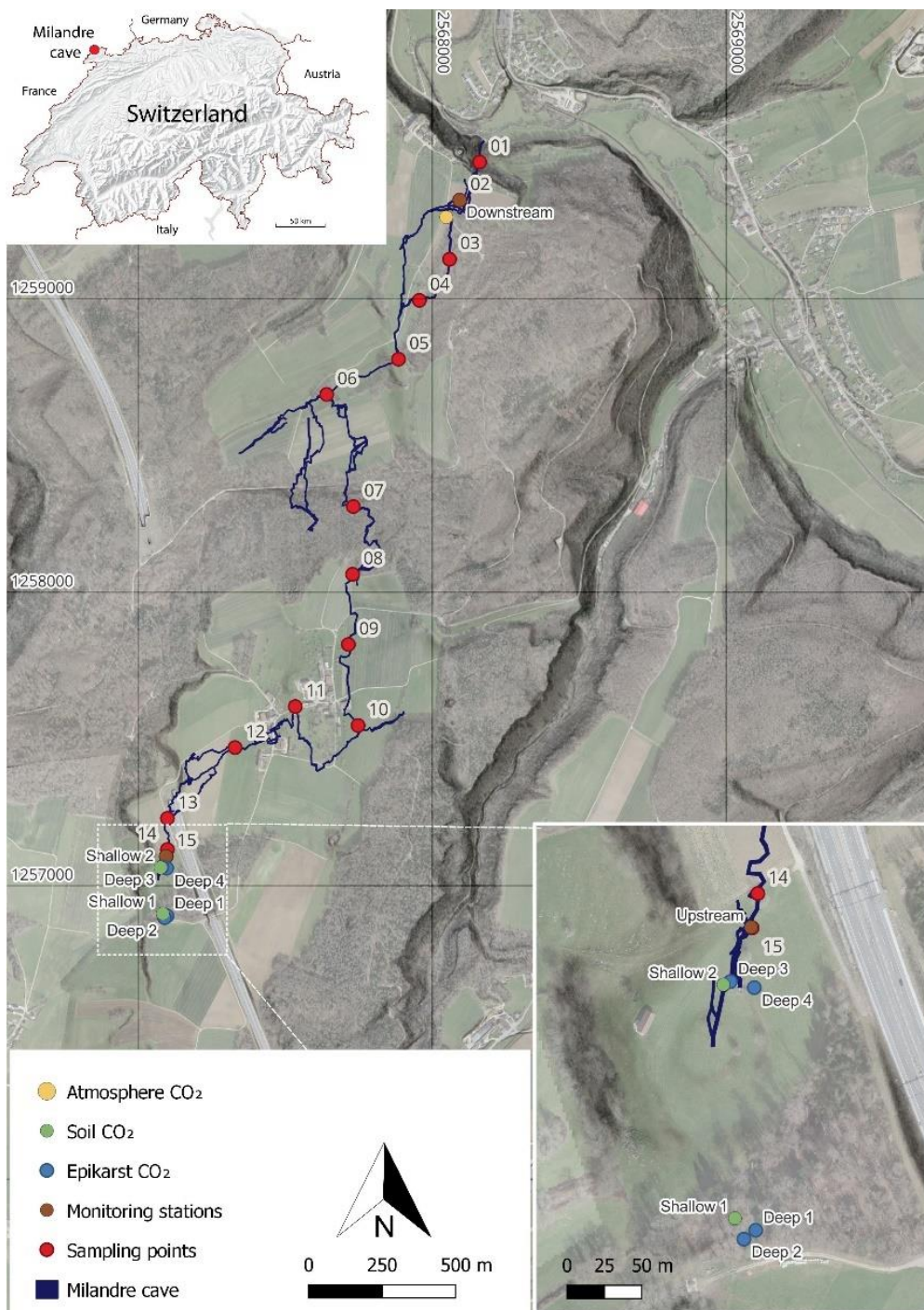
60



65 Though there has been extensive work investigating unsaturated zone CO₂ reservoirs, questions remain about the concentration, composition and sources of ground air on temporal and spatial scales. This study seeks to address this gap by presenting a detailed assessment of CO₂ concentrations and isotopic compositions over 2 years within the Milandre cave karst system in Switzerland. We aim to 1) Determine the relationships between pCO₂, δ¹³CO₂, and ¹⁴CO₂ in Milandre cave and its catchment; 2) Assess the effect of seasonality on CO₂ concentration and isotopic characteristics and 3) Gain insights into the provenances of CO₂ and how these evolve over time.

70 **2 Site Overview**

Milandre cave (47.4852 ° N, 7.0161 ° E, 373m a.s.l.) is located in the municipality of Boncourt in the Jura canton, NW Switzerland (Fig. 1). The Milandre karst structure formed within the Jura mountains, a sub-alpine mountain range which lies laterally in a northwest-southeast direction. The cave is located within the external Plateau unit of the Jura mountains which consists of thin sub horizontal Mesozoic limestone units that have experienced deformation which produced imbricates and tear faults (Sommaruga, 2011). More specifically, the Milandre karst system formed within the St-Ursanne Formation which overlies Oxfordian marls (Jeannin, 1998). The unsaturated zone ranges between 40 and 80 m depth, with a saturated zone of ~ 20 m (Perrin et al., 2003). The cave formed over 2.7 km, with 10.5 km of galleries forming along N-S oriented fractures. The Milandre river flows for 4.5 km in a northerly direction in the lower part of the cave and exits via the perennial Saivu spring where it joins the Allaine River, and the Bame temporary spring. The Milandre river drains a catchment area of approximately 13 km² (Perrin et al., 2003). There is a series of dolines in the catchment area which form depressions of ~10 to 20 m in the landscape. Notably, one doline is located in the meadow partially covering the upstream section of Milandre cave.



85 **Figure 1.** Map of the main passages of the Milandre cave network. The location of the atmospheric sampling (yellow), the soil (green) and epikarst boreholes (blue), and the cross-trip sampling (red) are annotated. Cave survey modified from Gigon & Wenger (1986). Base map from ©swisstopo.



Over the past 40 years, land use in the catchment area has been dominated by farmland (37 %), forest (36 %), and meadows (12 %) as estimated by aerial photo analysis (Jeannin et al., 2016). The crops grown primarily include maize and tobacco, two C4 plants. Long-term land use analysis shows that farmland has decreased slightly in this area and special infrastructures have increased due to the construction of a motorway that overlies part of the cave. The soils of the area are influenced by the ecosystem that is overlying it. Forest soils are shallow leptosols (< 10 cm deep) that are rich in fragments of the carbonate bedrock. The shallow forest soils transition into deeper (up to ~ 80 cm) organic rich histosols in the meadows, particularly in the dolines.

The Jura region experiences a marine west coast, warm summer climate (Cfb classification) (Kottek et al., 2006). Daily temperature measurements from the Fahy MeteoSwiss weather station located ~ 9.5 km SW from Milandre cave show an average temperature of 9.4 °C (1991 to 2020). Temperature seasonality is strong, with monthly average temperatures fluctuating between a minimum of -1.2 °C in January and a maximum of 18.2 °C in July from 1991 to 2020 (MeteoSwiss, 2024). In contrast, temperatures within the cave remain almost constant year-round, and vary between 10.3-11.0 °C (Affolter et al., 2020). The temperature difference between the outside and in-cave temperature drives dynamic ventilation on seasonal scales (Garagnon et al., 2022). Regional meteoric precipitation shows an average of 1046 mm year⁻¹. Monthly precipitation data indicate that precipitation in this area is well dispersed throughout the year (MeteoSwiss, 2024). Monitoring of tritium (³H) in stalagmite drip water was used to estimate the residence time of seepage water at ~ 5.5 to 6.6 years (Affolter et al., 2020).

3 Materials and methods

3.1 Gas sampling set up

All gas samples were taken every two months from December 2021 to January 2024. The samples were collected in 5 L sampling bags (Cali-5-Bond, Calibrated Instruments, USA) using a handheld pump. The gas was dried through a glass tube filled with granular magnesium perchlorate (~ 83 % purity, Supelco, Germany) to reduce the effects of humidity which may affect the isotopic composition of the sample. The sampling set up and procedure were identical for all gas samples. The CO₂ concentration was monitored during line flushing using an in-house built NDIR CO₂ sensor (SCD30, Sensirion, Switzerland) to ensure accurate sampling. The magnesium perchlorate was exchanged before each sampling day. Prior to analysis, the samples were stored away from direct sunlight in cool temperatures for a maximum of six weeks. The same bags were reused for each sampling location and were flushed with N₂ gas for at least 48 h before sampling to reduce cross contamination risks.

Atmospheric samples were collected at a defined sampling site above the cave (Fig. 1). Before sampling, the line was manually flushed for 1 min. To reduce the risk of breath contamination, the sampling set up was attached to 3 m long Teflon tubes, and samples were always taken against air flow direction.



120

The unsaturated zone air was sampled from six boreholes of varying depths between 0.5 and 5 m (Table 1). Spatially, the boreholes cover a large portion of the cave's upstream hydrological catchment, and are overlain by contrasting vegetation cover (mixed-deciduous forest or a grass meadow) (Fig. 1) (Table 1). The gas was sampled in two lines from depths of 0.5 to 0.85 m (Shallow 1), and three lines from 0.6 to 1.5 m (Shallow 2), and from deeper depths in single lines of 5 m (Deep 1, Deep 2, Deep 3, Deep 4). Due to the nature of the installation, it was not possible to assign a specific depth to the multi-line boreholes. All boreholes were drilled in 2013 and are equipped with aluminium tubes compacted by layers of gravel, bentonite and sand. The sampling line was flushed for 1 min once attached to the borehole, and then samples were taken into the Cali-5-Bond bags. Due to the nature of the borehole installation, we assume that the samples were not taken in steady state conditions, where the production rate of CO₂ would equal the sampling rate.

130

ID	Well names	SISKA ID	Easting (CH1903+/LV95) (Swiss grid)	Northing (CH1903+/LV95) (Swiss grid)	Depth (m)	Number of sampling lines	Classification	Ecosystem cover
SG-04	Shallow 1	CO2-13	2'567'083	1'256'904	0.5 to 0.85	2	Soil	Forest
SG-07	Shallow 2	CO2-10	2'567'074	1'257'068	0.6 to 1.5	3	Soil	Meadow
SG-05	Deep 1	EPI-2	2'567'097	1'256'896	5	1	Epikarst	Forest
SG-10	Deep 2	EPI-4	2'567'089	1'256'890	5	1	Epikarst	Forest
SG-08	Deep 3	EPI-7	2'567'080	1'257'063	5	1	Epikarst	Meadow
SG-09	Deep 4	EPI-5	2'567'096	1'257'059	5	1	Epikarst	Meadow

Table 1 Summary of the boreholes sampled in Milandre cave catchment notating sample depth, number of sampling lines, classification in soil/ epikarst zone, and ecosystem cover type. The ID's are the names given to the boreholes for this study, and are concurrent with the supplementary data provided. SISKA (Swiss Institute for Speleology and Karst Studies) IDs refer to the original names of the boreholes at the time of installation.

135

Cave air was sampled in two locations within Milandre cave proximal to both entrances, Downstream (topographically lower) and Upstream (topographically higher), with the same procedure as for the atmospheric samples (Fig. 1). To gain insight into possible spatial variability within the cave, a cross-trip through the main passage of the cave was carried out in September 2021, and 14 samples were collected (Fig. 1). The trip was taken against the direction of air flow, from the downstream to upstream entrance, again to reduce risk of breath contamination.

140



3.2 Continuous O₂ and CO₂ concentration monitoring

Soil gas O₂ and CO₂ concentrations were measured continuously nearby Shallow 2 at 40 cm depth and recorded at 10 min intervals between April 2023 and June 2024 using a SCD-41 CO₂ sensor (± 50 ppmV + 5 % of reading) (Sensirion, Switzerland) and SGX-40X O₂ sensor (Amphenol SGX, Sensortech, Switzerland). Calibration was cross-checked with an independent, handheld multi-gas monitor (XAM 5600, Dräger, Germany) before installation.

3.3 CO₂ concentration and $\delta^{13}\text{C}$ analysis

The concentration of CO₂ and the stable carbon isotopic composition ($\delta^{13}\text{C}$) in all gas samples was measured using a cavity ringdown spectrometer (CRDS) G2131-I Isotopic CO₂ instrument (Picarro, USA) at ETH Zurich (CO₂ concentration = 0.2 ppm, $\delta^{13}\text{C} = < 0.1$ ‰ precision). Standard gases with known CO₂ concentrations, 399.6 ppmV and 2000 ppmV CO₂ in synthetic air, were measured in addition to standard gases of known $\delta^{13}\text{C}$ values, -27.8 ‰ and -2.8 ‰ VPDB, for offline calibration. As there was no standard gas available for similarly high CO₂ concentrations as in some samples, linearity of the concentration data produced by the CRDS is assumed. All standards and samples were measured by directly attaching the sample bags to the inlet of the CRDS that was previously fitted with a magnesium perchlorate dryer, and measuring gas concentration and isotopic composition for 2 min after reaching steady state. For the evaluation, we used the mean and standard deviation of this measurement interval. $\delta^{13}\text{C}$ refers to the ratio between the two stable carbon isotopes with respect to the Vienna Pee Dee Belemnite (VPDB) standard:

$$\delta^{13}\text{C} (\text{‰}) = \left(\frac{{}^{13}\text{C}/{}^{12}\text{C}_{\text{sample}}}{{}^{13}\text{C}/{}^{12}\text{C}_{\text{standard}}} - 1 \right) \times 1000 \quad (1)$$

3.4 Radiocarbon analysis

The CO₂ from each gas sample was converted into approximately 1 mg of graphite using an Automatic Graphitization Equipment (AGE, IonPlus, Switzerland) (Wacker et al., 2010a) coupled with a custom-made carbon inlet system. In this process, each sampling bag was successively attached to the inlet system which dried the sample through a fine-grained magnesium perchlorate water trap via a vacuum line. The volume of air required to sample was calculated depending on the CO₂ concentration of the sample, and the appropriate amount was trapped within a stainless-steel coil that was cooled by submersion in a liquid N₂ bath. After trapping, the CO₂ was sublimated by submerging the coil in a room temperature water bath and then adsorbed onto a zeolite trap using helium as a carrier gas between the coil and the trap. The CO₂ adsorbed onto the trap was then thermally desorbed and filled into the AGE reactor, where it was reduced to graphite with hydrogen over an iron catalyst (Wacker et al., 2010a). Oxalic Acid II gas (F¹⁴C = 1.3407, Oxa II, NIST SRM 4990C, HEKAL AMS Lab, Hungary) as a modern standard and a radiocarbon fossil reference CO₂ gas (F¹⁴C = 0, CO₂ ≥ 99.7 % Vol.abs, Carbagas, Switzerland) were also graphitized and used to calibrate the measurements. The resulting graphite was pressed into targets for



175 radiocarbon analysis through AMS analysis with a MIni CARbon DAting System (MICADAS, Ionplus, Switzerland) (Synal
et al., 2007; Szidat, 2020). The resultant radiocarbon data were corrected using the BATS (4.3) software (Wacker et al., 2010b).
In this study the ^{14}C content of samples will be discussed in $F^{14}\text{C}$ notation according to Reimer et al., (2004):

$$F^{14}\text{C} = \frac{{}^{14}\text{C}/{}^{12}\text{C}_{\text{sample}}}{{}^{14}\text{C}/{}^{12}\text{C}_{\text{standard}}} \quad (2)$$

180 3.5 Dissolved inorganic carbon analysis

Drip water dissolved inorganic carbon (DIC) ^{14}C was measured to constrain the DIC degassing endmember. Samples were
measured over one year from December 2021 and December 2022 at 9 drip sites focused on the actively dripping galleries
nearby Upstream and Downstream (Fig. 1). Using a 5 mL syringe, 1 mL of drip water was collected directly from the soda
straw stalactites on the cave roof to reduce fractionation effects associated with degassing. The water was injected directly into
185 pre-cleaned Exetainer® (Round Bottom, Borosilicate, 938W, Labco Limited, UK) vials which had been flushed with helium
gas and pre-spiked with 150 μL of 85 % H_3PO_4 (Suprapur®, 85 %, Merck KGaA, Germany). The ^{14}C content of the DIC was
measured by sampling the vial headspace using the Carbonate Handling System (CHS, Ionplus, Switzerland) and transferring
the gaseous sample to the AMS using a gas handling system. Here, the CO_2 was introduced to the gas ion source through the
CHS at a flow of 50 mL min^{-1} . The ^{14}C content for each sample was measured for ~ 60 cycles. Standard material with a
190 carbonate matrix of similar composition to the DIC samples were used as standards (IAEA C1 ($F^{14}\text{C} = 0$) and C2 ($F^{14}\text{C} =$
0.411), sodium bicarbonate (NaHCO_3 , Sigma Aldrich, USA) and potassium bicarbonate (KHCO_3 , Sigma Aldrich, USA) (both
 $F^{14}\text{C} = 0$)).

3.6 Data analysis and statistics

195 All data and statistical analyses and all graphs were generated using the Python 3 programming language (Van Rossum &
Drake, 2009).

Relationships between CO_2 concentration, $\delta^{13}\text{C}$, $F^{14}\text{C}$ for each sample type and the Mean Monthly Temperature (MMT) and
200 Mean Monthly Precipitation (MMP) from Fahy weather station were explored using Spearman's rank correlation coefficient
analysis (Kokoska & Zwillinger, 2000). A significantly correlated relationship between two variables is defined by $p < 0.05$,
with the correlation coefficient denoted by “ ρ ”, and number of samples involved in the analysis as “ n ”.

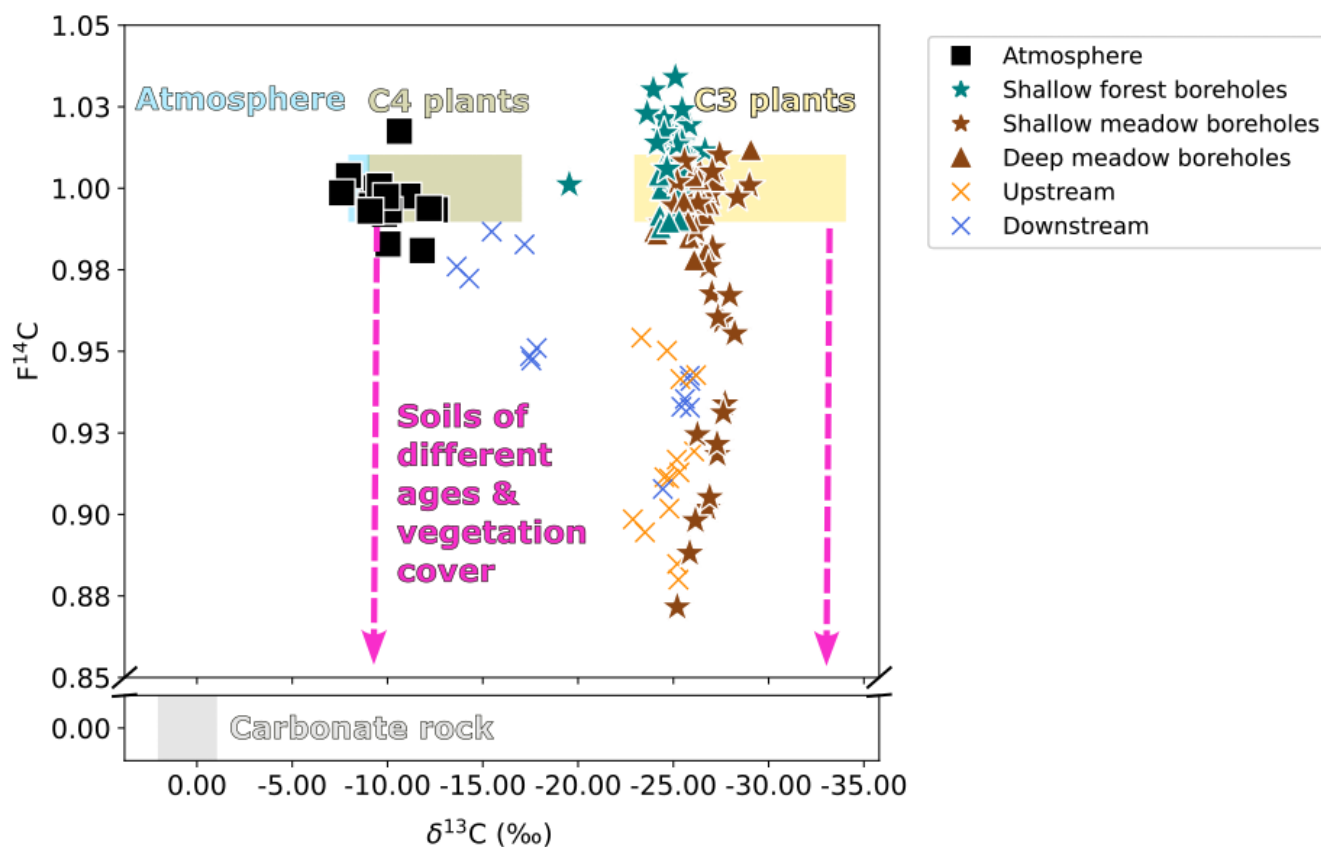


4 Results

205 4.1 Atmospheric CO₂

The atmospheric samples had a CO₂ concentration ranging from ~ 380 ppmV (August 2023) to ~ 485 ppmV (December 2022) with an average of ~ 440 ppmV. The $\delta^{13}\text{C}$ ranged from -12.5 ‰ (February 2023) to -7.6 ‰ (August 2023) and had a mean of -10.1 ‰ (n = 17). The CO₂ sampled was typically modern, though had some fluctuation from F¹⁴C 0.98 (December 2022) to 1.02 (June 2022) and a mean of F¹⁴C 1.0 (Fig. 2).

210



215

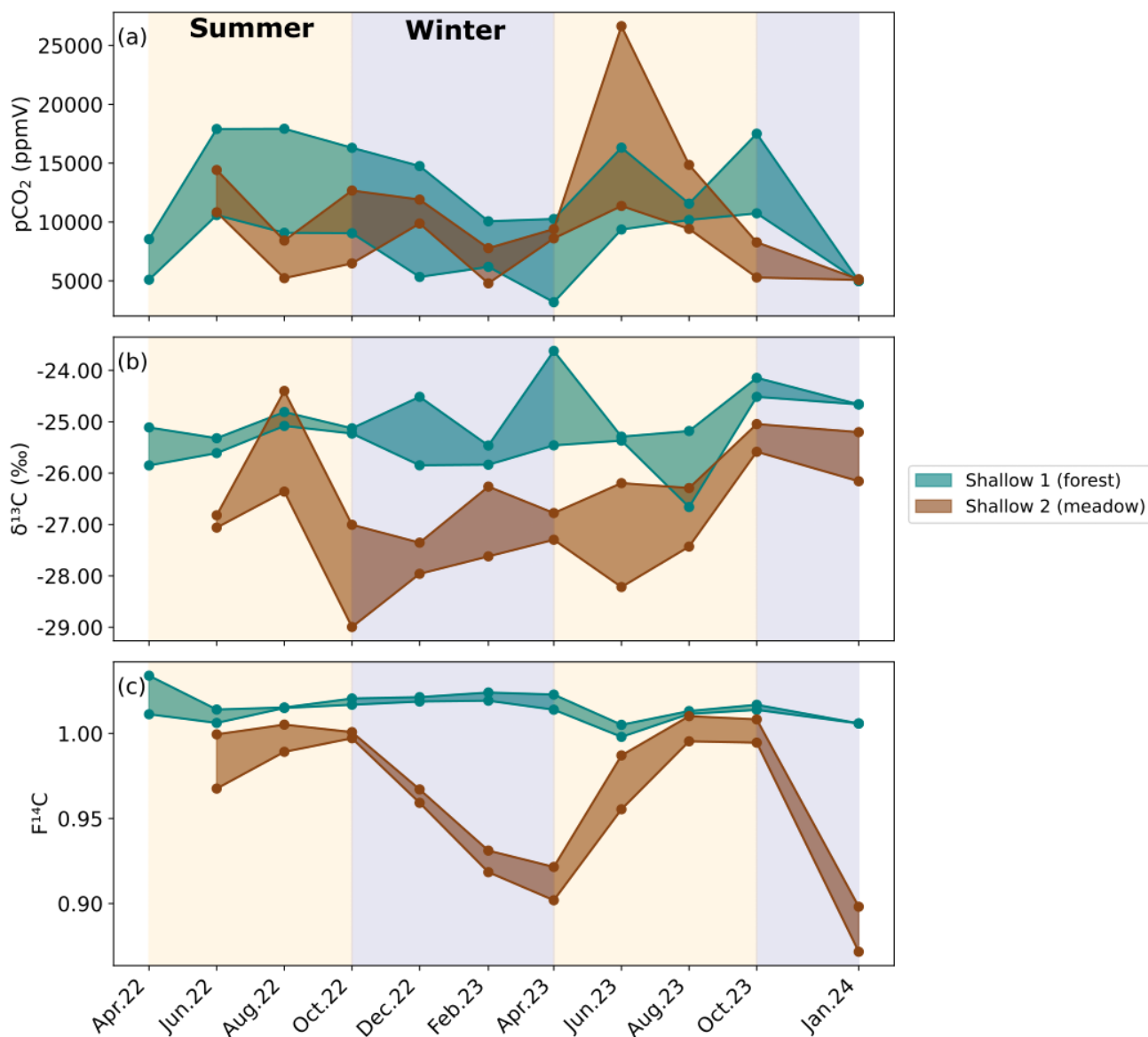
Figure 2. $\delta^{13}\text{C}$ and F¹⁴C of all gas samples over the monitoring period. The theoretical carbon reservoirs present in the system are shown with the atmosphere (blue), C3 plants (yellow), C4 plants (green), soils of various ages and compositions (pink arrows), and carbonate rock (grey).



220 4.2 Soil Zone CO₂

Soil boreholes have higher CO₂ concentrations and lower δ¹³C compared to the atmosphere (Fig. 2). Concentrations in boreholes that sample the soil zone (Shallow 1 and Shallow 2) (Fig. 3a) vary significantly depending on sampling depth, cover type, and season. The Shallow 1 boreholes (forest) show seasonal high pCO₂ in the summer months from June to October, which steadily declines during winter until it begins to rise again after April. The Shallow 1 (forest) boreholes vary from a maximum of ~ 18'000 ppmV in August 2022 to a minimum in January 2024 of ~ 1200 ppmV, with an average of ~10'700 ppmV (n = 21). The Shallow meadow boreholes range from ~ 27'000 ppmV in June 2023 to ~ 4800 ppmV in February 2023 with an average of ~ 9900 ppmV (n = 30).

The δ¹³C varies by 7.0 ‰ in shallow forest boreholes over the sampling period ranging from a minimum of -26.7 ‰ in August 2023 to a maximum of -19.5 ‰ in January 2024 (Fig. 3b). There is 4.0 ‰ isotopic variation in the shallow meadow boreholes with a minimum of -29.0 ‰ in October 2022 and a maximum of -24.4 ‰ in August 2022. The pCO₂ and δ¹³C are negatively correlated in both shallow forest and shallow meadow boreholes (forest: ρ = -0.47, p = 0.02, n = 25. meadow: ρ = -0.49, p = 0.01, n = 30), and δ¹³C is on average lower in shallow meadow than shallow forest boreholes.



235

Figure 3. Maximum and minimum a) CO₂ concentration, b) δ¹³C and c) F¹⁴C of soil borehole samples from Shallow 1 in the forest (green) and Shallow 2 in the meadow (brown). Summer (yellow) and winter (blue) seasons are highlighted by the coloured background. Concentrations are shown as ranges between maxima and minima as they aggregate over several sampling lines in the soil per location (Table 1).

240



F¹⁴C in Shallow 1 boreholes (forest) shows little annual variability and fluctuates slightly around a modern value (max = 1.03 in April 2022, min = 1.0 in June 2023) (Fig. 3c). Conversely, the shallow meadow boreholes show distinct annual variation in F¹⁴C, which steadily decreases from modern (1.0) in August 2022 and 2023 to a low in April 2023 and a minimum in January 2024 (0.87). The samples from the shallow forest boreholes have a positive correlation between F¹⁴C and δ¹³C ($\rho = 0.48$, $p = 0.02$, $n = 25$). In the shallow meadow borehole samples, we observe a positive correlation between F¹⁴C and MMT ($\rho = 0.67$, $p = 0.001$, $n = 30$). All other tested parameters show no significant correlations (see Appendix A).

The continuously measured O₂ and CO₂ concentrations nearby Shallow 2 in the meadow show an inverse relationship (Fig. 4). The concentrations are relatively stable throughout most of the year with higher O₂ and lower CO₂ concentrations. This pattern is disturbed by a sharp decrease in O₂ and an increase in CO₂ observed around May/June of both 2023 and 2024. These different conditions last around one month before returning to the typical concentrations. The O₂ concentration ranges from a maximum of 20.2 % in August 2023 to a minimum of 17.8 % during a brief interval in May 2023. Conversely, the CO₂ concentration peaks at ~ 17'000 ppmV in May 2023 and is the lowest at ~ 2500 ppmV in August 2023. The Shallow 2 boreholes also show peaks in CO₂ concentration in May to June 2023 (Fig. 4).

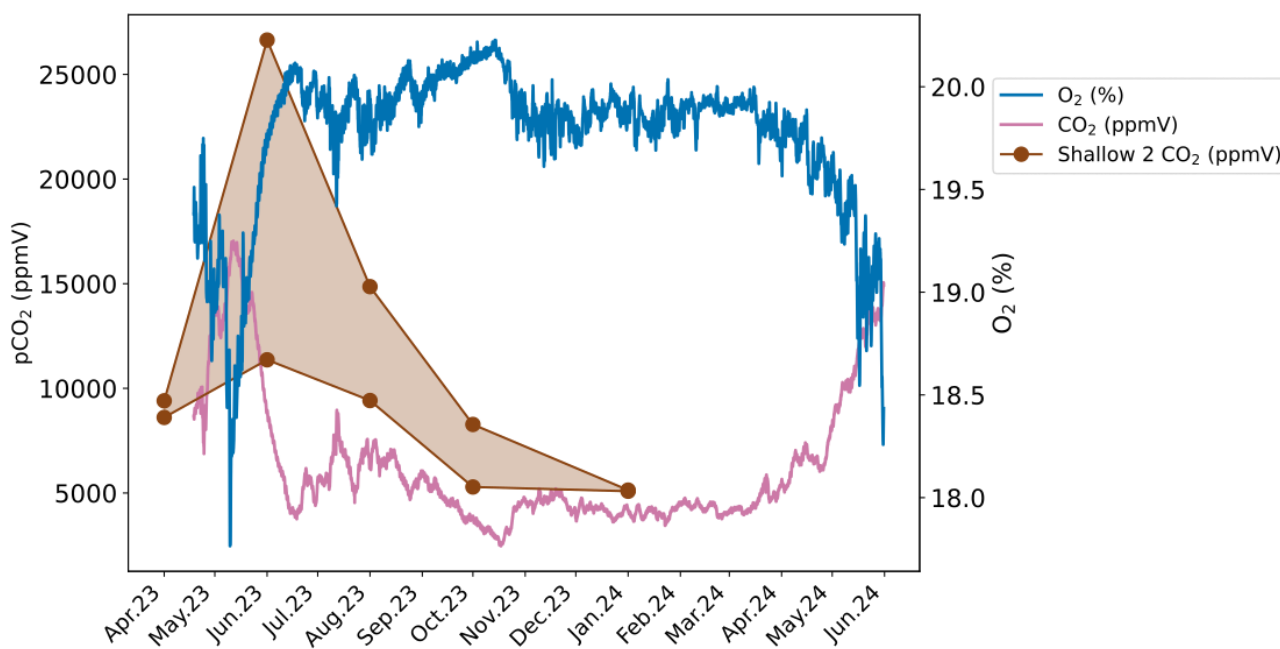


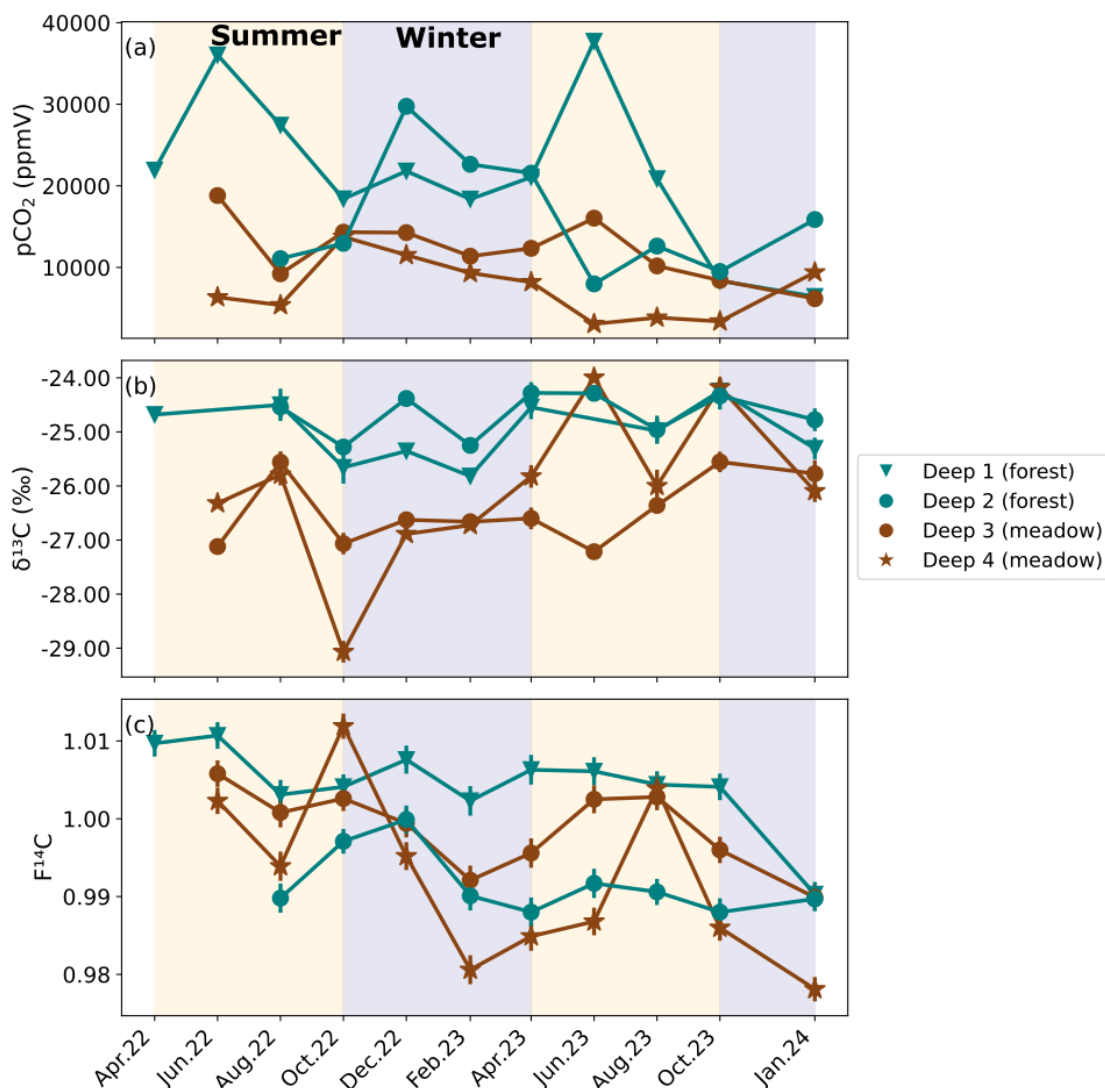
Figure 4. Continuously measured CO₂ (pink) and O₂ (blue) concentrations from the soil zone nearby the Shallow 2 boreholes. CO₂ concentrations from Shallow 2 are also plotted (brown).



4.3 Epikarst CO₂

Epikarst CO₂ concentrations varied widely during the sampling period but generally are very high (>10'000 ppmV). On average, the forest boreholes Deep 1 and Deep 2 have higher concentrations than the meadow boreholes Deep 3 and Deep 4. Concentrations are generally highest in the Deep 1 borehole (forest) (Fig. 5a) with a maximum of ~ 37'000 ppmV in June 2023 and a similarly high concentration peak in June 2022. The lowest values (~ 21'000 ppmV) at this borehole are recorded in the winter months. Deep 2 (forest) shows an opposite trend with its highest CO₂ concentrations in autumn, winter, and spring (max = ~ 29'000 ppmV in December 2022). The lowest CO₂ concentrations were measured during the summer months (min = ~ 7900 ppmV in June 2023). There is comparatively less variability in the Deep 3 and Deep 4 boreholes (both in the meadow). In Deep 3, concentrations fluctuate from ~ 6100 to ~ 19'000 ppmV with no obvious seasonality. Deep 4 has higher concentrations over the winter period and lower during summer, peaking at ~ 14'000 ppmV in October 2022 and dropping to an overall minimum of ~ 3000 ppmV in June 2023.

The $\delta^{13}\text{C}$ of the majority of epikarst CO₂ samples is very stable around ~ -26 ‰ (Fig. 5b). Similar to the shallow boreholes, samples from deep meadow boreholes (Deep 3 and 4) have on average slightly lower $\delta^{13}\text{C}$ values. In the meadow boreholes Deep 3 and Deep 4, the $\delta^{13}\text{C}$ and pCO₂ are negatively correlated ($\rho = -0.66$, $p = 0.001$, $n = 21$) (see Appendix A).



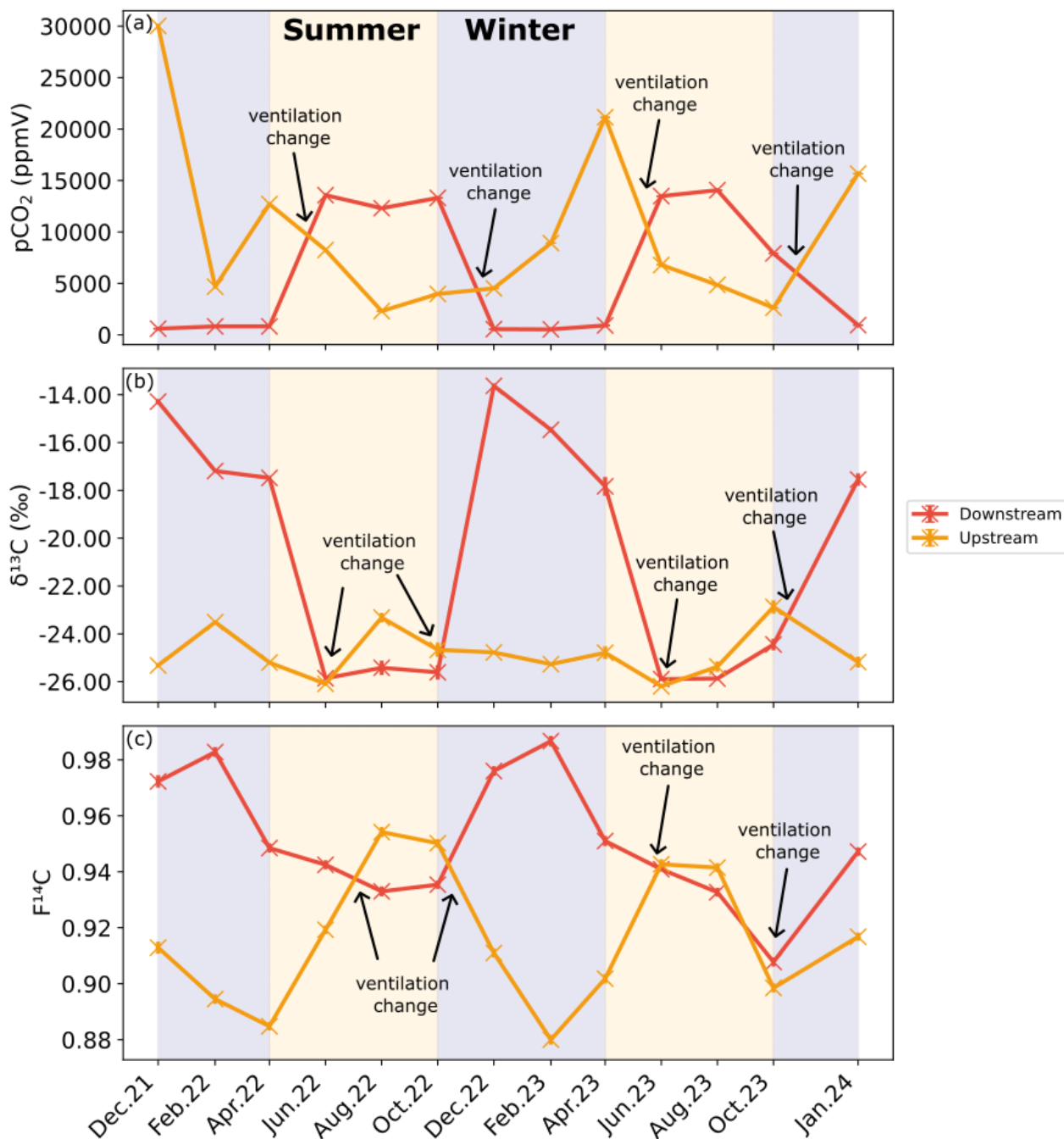
280 **Figure 5. a) CO₂ concentration, b) δ¹³C and c) F¹⁴C of epikarst borehole samples from forest boreholes Deep 1 and Deep 2 (green), and meadow boreholes Deep 3 and Deep 4 (brown). Summer (yellow) and winter (blue) seasons are highlighted by the coloured background.**

The F¹⁴C of epikarst CO₂ samples is relatively stable throughout the sampling period, ranging from 1.01 (Deep 1, June 2022) to 0.98 (Deep 4, October 2022) (Fig. 5c). A possible seasonal pattern can be observed in the meadow boreholes (Deep 3 and Deep 4) with lower F¹⁴C values in the winter and spring months and higher F¹⁴C during summer, similar to the observation
285 from the shallow meadow boreholes. No clear seasonal pattern is observed for Deep 1 and Deep 2. The F¹⁴C epikarst CO₂ samples are negatively correlated with their δ¹³C value ($\rho = -0.54$, $p = 0.01$, $n = 21$) and positively correlated with MMT ($\rho = 0.53$, $p = 0.01$, $n = 21$). All other tested parameters show no significant correlations.



4.4 Cave CO₂

290 The CO₂ concentrations at the Downstream and Upstream sampling points in the cave are inversely correlated (Fig. 6a).
Downstream shows higher pCO₂ from June to October in 2022 and 2023, with a maximum of ~ 14'000 ppmV in August 2023.
The lowest concentrations are seen between December and April, reaching close to atmospheric concentrations with a
minimum of ~ 420 ppmV in December 2021. Conversely, the highest CO₂ concentrations at the Upstream site were measured
during the winter months, with a maximum of ~ 30'000 ppmV in December 2021. The lowest CO₂ concentrations at Upstream
295 were observed during the summer months with a minimum of ~ 2300 ppmV in August 2022. Overall, concentrations at the
Upstream site reach higher maxima and do not approach atmospheric values at their minimum, as at the Downstream site. The
isotopic composition of CO₂ is inversely related to its concentration, with higher CO₂ concentration coinciding with lower
F¹⁴C and δ¹³C values. Seasonal trends differ between sites, at the Downstream site δ¹³C and F¹⁴C values are higher in winter
and lower in summer, whereas at the Upstream site, δ¹³C and F¹⁴C values show the opposite patten (Fig. 6b and c). The δ¹³C
300 in Downstream ranged between -25.9 ‰ in June 2023 and -13.6 ‰ in December 2021, and the F¹⁴C between 0.91 in October
2023 and 0.98 in February 2023. At Upstream, the opposite relation with CO₂ concentration is well expressed for F¹⁴C, but not
as clear for δ¹³C, with minimal variability over the entire study period. The δ¹³C in Upstream fluctuates slightly around a mean
of -24.8 ‰.



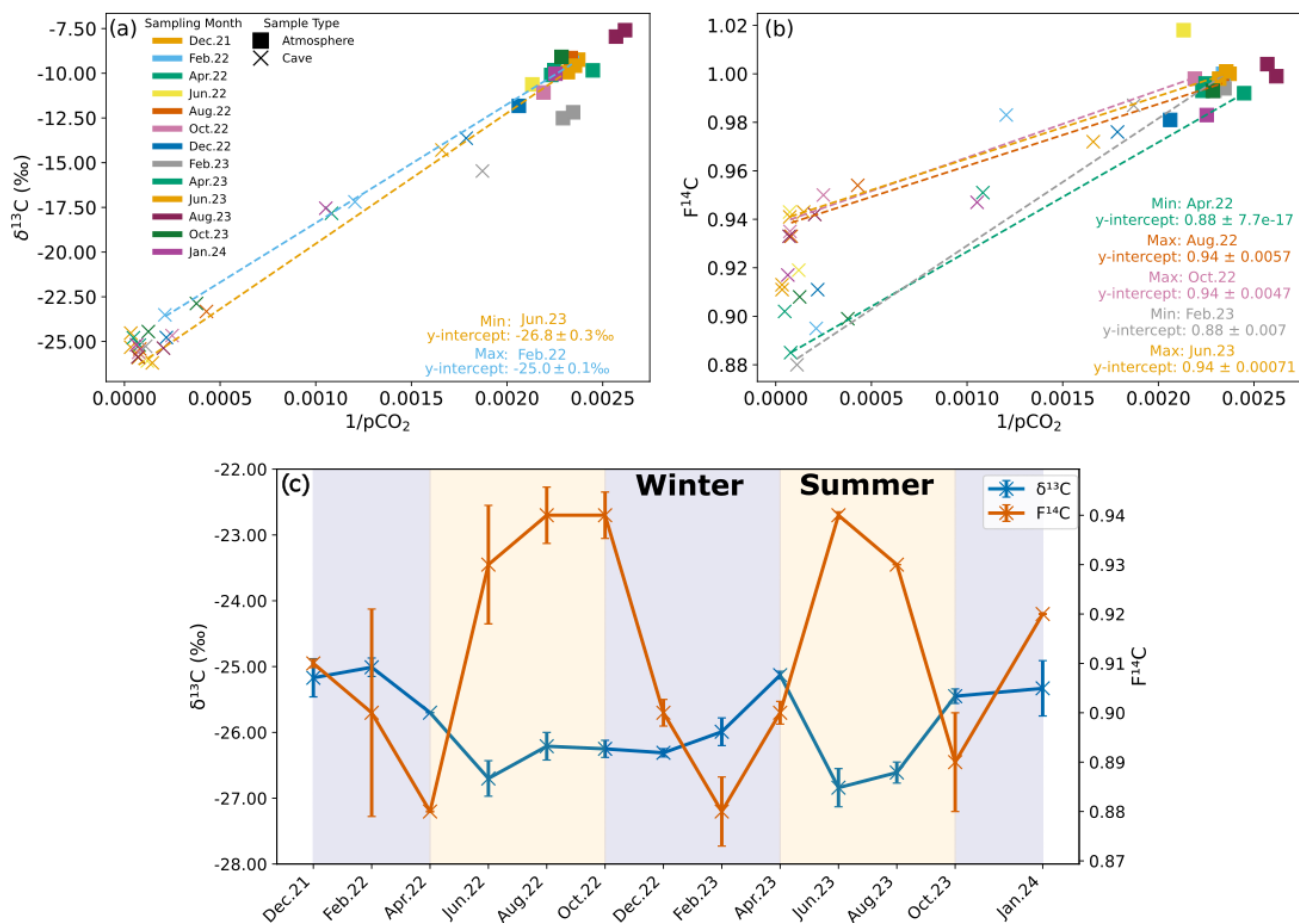
305

Figure 6. a) CO₂ concentration, b) δ¹³C and c) F¹⁴C of cave air samples from the Downstream (red) and Upstream (orange) sites. Summer (yellow) and winter (blue) seasons are highlighted by the coloured background. The approximate timing of the temperature driven ventilation direction changes are shown by the annotations.



310 The $F^{14}C$ of CO_2 in Upstream is overall lower than that of Downstream, increasing over late spring 2022 and into summer, peaking during August 2022 at 0.95. Decreasing $F^{14}C$ is observed during winter into spring with lows of ~ 0.88 in February 2023. At the Downstream site, the pCO_2 and $\delta^{13}C$ ($\rho = -0.9$, $p = 0.0001$, $n = 14$), pCO_2 and $F^{14}C$ ($\rho = -0.83$, $p = 0$, $n = 14$), and $\delta^{13}C$ and MMT ($\rho = -0.79$, $p = 0.0001$, $n = 14$) are negatively correlated. Moreover, the pCO_2 and MMT ($\rho = 0.53$, $p = 0.05$, $n = 14$), and $\delta^{13}C$ and $F^{14}C$ ($\rho = 0.74$, $p = 0$, $n = 14$) are positively correlated. At the Upstream site, pCO_2 and MMP are positively
315 correlated ($\rho = 0.55$, $p = 0.04$, $n = 14$), and pCO_2 and MMT are negatively correlated ($\rho = -0.54$, $p = 0.05$, $n = 14$) (See Appendix A). All other tested parameters show no significant correlations.

To constrain the isotopic composition of the end members contributing CO_2 to the cave air mixture, we use the Keeling plot approach (Fig. 7a & b). This approach assumes that cave air is a mixture of two main sources, the atmosphere (with known
320 concentration and isotopic values), and a second source of a priori unknown composition. The y-intercepts of the Keeling plots represent the isotopic composition of the contributing end member which mixes with atmospheric air inside the cave (Keeling, 1961; Pataki et al., 2003) (Fig. 7a & b). We find that over time, the isotopic composition of the endmember varies for both $\delta^{13}C$ and $F^{14}C$ (Fig. 7c). The endmember $\delta^{13}C$ value varies slightly by ~ 2.0 ‰ from -26.8 ‰ in June 2023 to -25.0 ‰ in February 2022. The variation in the $F^{14}C$ is larger, ranging from 0.88 in February 2023 to 0.94 in June 2022, August 2022,
325 October 2022, and June 2023 (ca. $\sim 0.06 F^{14}C$). Maxima in the $F^{14}C$ value derived for the endmember through the Keeling plot generally correspond to decreases in $\delta^{13}C$, with two $F^{14}C$ maxima occurring in June to October 2022 and in June to August 2023.



330

Figure 7. Keeling plots for $\delta^{13}\text{C}$ (a) and $F^{14}\text{C}$ (b) of cave (Upstream and Downstream sites) and atmospheric samples from all monitored months. The dashed regression lines denote the months with the maximum and minimum y-intercepts for $\delta^{13}\text{C}$ and $F^{14}\text{C}$. c) Keeling plot y-intercepts for $\delta^{13}\text{C}$ (blue) and $F^{14}\text{C}$ (orange) over time. Summer (yellow) and winter (blue) seasons are highlighted by the coloured background.

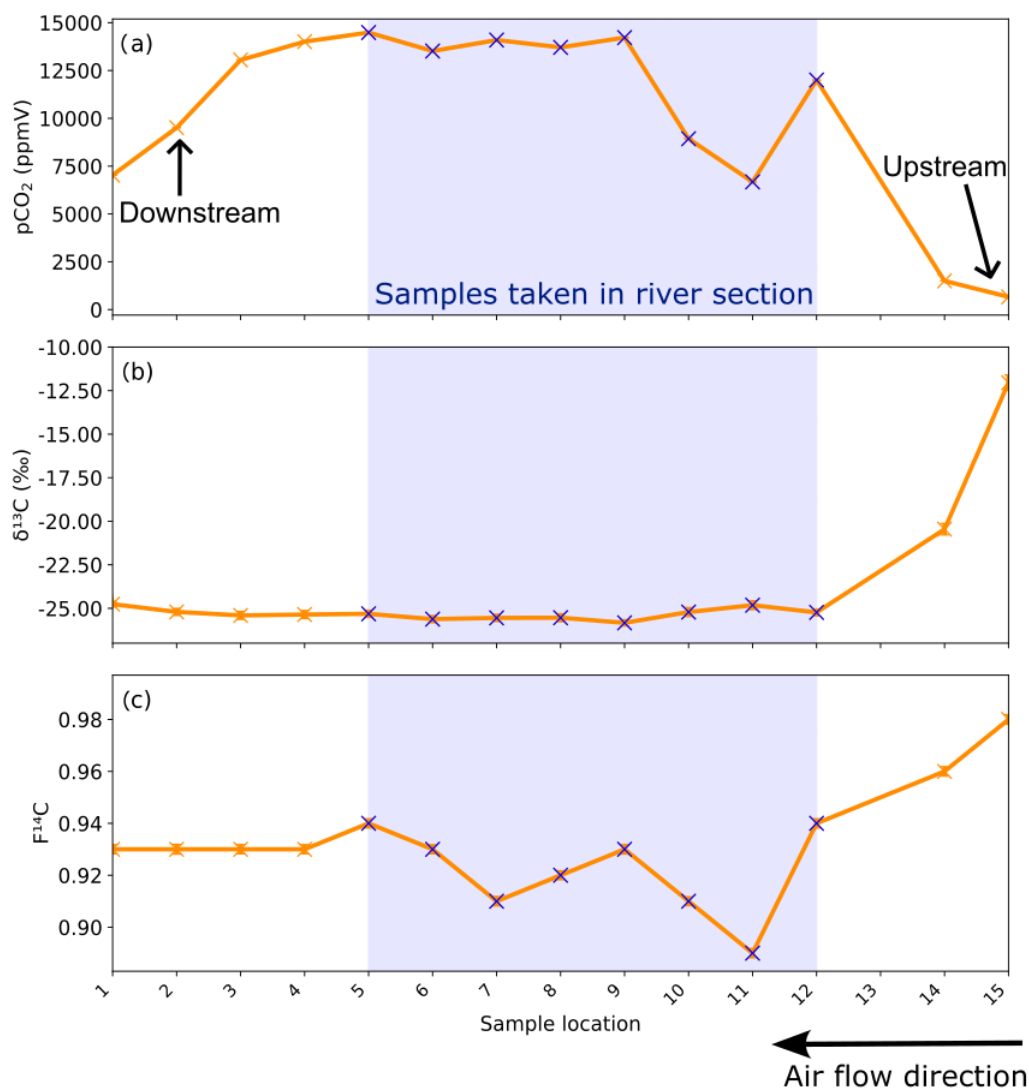
335

Samples taken along the main passage of the cave during the cross-trip show increasing $p\text{CO}_2$ from the lower entrance (location 1, corresponding to Downstream monitoring site, ~ 6900 ppmV) to a plateau of $\sim 14'000$ ppmV from sample point 4 to 9 towards the centre of the cave (Fig. 8a). The $p\text{CO}_2$ decreases sharply after sample point 9 until point 11 (~ 6600 ppmV). The $p\text{CO}_2$ then increases briefly at sample point 12 and then decreases again upon approach to the cave exit (Upstream). The $\delta^{13}\text{C}$ values remain essentially constant at -25.5 ‰ through the initial segments of the cave, beginning to increase slightly past sample point 9 (Fig. 8b). The $\delta^{13}\text{C}$ value is -25.8 ‰ at sample point 9 and progressively increases as $p\text{CO}_2$ levels drop between sampling points 9 and 11, followed by a strong increase toward the Upstream exit (-11 ‰). The $F^{14}\text{C}$ values are constant at ~ 0.93 between sample points 1 and 5, followed by more variability and generally lower $F^{14}\text{C}$ values in the middle of the transect,

340



coinciding with the river passage of the cave (minimum 0.89 at sampling point 11; Fig. 9c). Towards the Upstream exit, $F^{14}C$ begins to increase strongly (maximum 0.98 at sampling point 15; Fig. 8c). Sample 13 is excluded due to a ruptured bag during sampling.



350 **Figure 8.** a) CO_2 concentration, b) $\delta^{13}C$ and c) $F^{14}C$ of cave air samples from the different sites sampled during the cross trip. Sampling locations are shown in Fig. 1. The blue crosses and blue bar notate where samples were taken standing in the river. The direction of cave air ventilation is shown by the lower arrow. The approximate locations of the Upstream and Downstream sampling sites are annotated.



5 Discussion

5.1 Sources and variability of shallow depth CO₂

355 The observed fluctuations in CO₂ concentrations in the Shallow boreholes (0.5 to 1.5 m) varying with depth, vegetative cover, and season suggest complex carbon cycling dynamics taking place in the soil zone and shallow fractured epikarst. Overall, both samples from forest and meadow locations have similar average CO₂ concentrations. In the Shallow 1 forest boreholes, higher CO₂ concentrations occur during summer months (Fig. 3a), aligning with increased autotrophic (occurring in plant roots, leaves, and stems) and heterotrophic (microbial) respiration rates during warmer seasons resulting in higher CO₂ production compared to losses due to soil efflux to the atmosphere and downward transport in gaseous or dissolved form. Due to our discrete sampling approach, we cannot discern between higher production and increased losses. The decline in CO₂ concentrations during winter indicates reduced soil microbial respiration, and reduced autotrophic respiration, in response to lower temperatures. Though CO₂ production is reduced in winter, concentrations of several ~1000 ppmV are measured at our sites, perhaps due to the ability of soil bacteria to survive in below freezing temperatures as low as -5 to -7.5 °C (Kähkönen et al., 2001), to persisting autotrophic respiration of shallow roots, or because of reduced transportation of CO₂ due to higher soil water content (Hashimoto & Komatsu, 2006). Similar seasonal trends in CO₂ concentrations have been observed in several other studies (Billings et al; 1998; Pumpanen et al., 2003; Zhang et al., 2023). Comparatively, CO₂ concentrations in the Shallow 2 meadow boreholes do not show as pronounced seasonality due to consistent CO₂ accumulation year-round.

370 δ¹³C of CO₂ in shallow boreholes located in both the meadow and forest correspond to the typical isotopic signature of C3 plants which dominate the catchment area, supporting our interpretation of a dominant biogenic source of carbon in the soil gas (Fig. 2) (Fig. 3b). Plants using the C3 metabolic pathway (e.g. most temperate vegetation) produce carbon with a δ¹³C of ~ -23 to -34 ‰ (Staddon et al., 2004). Furthermore, due to the nature of the sampling, the soil was not sampled in steady state conditions, potentially disturbing any existing CO₂ trends with depth. Though both meadow and forest boreholes have C3 plant δ¹³C signatures, the δ¹³C of the meadow soils are on average lower than those in the forest soils. The meadow and forested areas have developed contrasting soil compositions, with the meadow soils deeper, more compacted, and with a higher organic content, whilst the forest soils are shallow, unconsolidated, and with more roots. Comparisons of root free and root containing soils have suggested that root respiration contributes lower δ¹³CO₂ to the soil gas (Diao et al., 2022). This is the opposite trend to what our findings would suggest. Efforts to disentangle the δ¹³C of autotrophic and heterotrophic contributions to soil CO₂ have shown a range of results, where autotrophic respiration can produce the same (Wu et al., 2017), higher (Moyes et al., 2010), or lower (Risk et al., 2012) δ¹³C than heterotrophic respiration. However, different soil compositions can affect soil moisture, which can cause both increases (Unger et al., 2010), decreases (Powers et al., 2010), and no change (Diao et al., 2022) in soil δ¹³C. It is therefore difficult in the context of this study to determine the exact reason for the difference in δ¹³C between surface covers. Interestingly, we also do not find evidence for contributions to subsurface gas from C4 plants, possibly



385 due to the absence of sampling locations in the fields in the catchment where C4 crops are grown, suggesting limited lateral
gas transport.

The CO₂ F¹⁴C of meadow boreholes in Shallow 2 shows statistically significant seasonal behaviour ($\rho = 0.67$, $p = 0.001$, $n =$
30), with more aged CO₂ dominating the winter and spring months (F¹⁴C ~ 0.88), and modern CO₂ in summer (F¹⁴C ~ 1.00)
390 (Fig. 3c). These seasonal shifts suggest a potential influence of temperature-sensitive processes on soil carbon dynamics, with
higher autotrophic respiration rates in the warm months, as well as heterotrophic respiration of very recently fixed
photosynthates dominating (Campeau et al., 2019). Though typically the productive growing season for meadow grasses occurs
in spring (Wingler & Hennessy, 2016), there is a lag in the response in the F¹⁴C, which peaks between June and October. This
may be due to the time it takes for enough modern CO₂ to accumulate in the soil and dominating the average gas age. Similar
395 impacts of seasonality on the contributions of young carbon pools to the soil CO₂ budget have been observed in soils of various
environments whereby autotrophic respiration and heterotrophic decomposition of younger carbon dominate in warmer months
(Trumbore, 2000; Chiti et al., 2011; Vaughn & Torn, 2018). A contribution of fossil carbon from the dissolution of carbonate
bedrock fragments in the soil zone could also be considered to explain the low soil CO₂ F¹⁴C values in winter. However, such
a bedrock contribution would result in a concomitant increase in $\delta^{13}\text{C}$, as marine carbonates, which typically constitute the
400 karstified host rock, are characterized by $\delta^{13}\text{C}$ of values of ~ 0 ‰ (Planavsky et al., 2015) and up to + 2 ‰ in the region of
Milandre cave (Weissert & Mohr, 1996) (Fig. 2), with a gaseous $\delta^{13}\text{C}$ ~ 9.54 ‰ lighter when at equilibrium with DIC from
carbonate dissolution at 10.5 °C (Mook et al., 1974). Since we do not observe increases in $\delta^{13}\text{C}$ of soil gas during the periods
of lower F¹⁴C, this is an unlikely scenario. A further explanation for the seasonal variability could be due to the seasonal
ventilation dynamics in the karst system, which promote upwards ventilation of cave air during the winter, and downwards
405 ventilation of soil air in summer (see section 5.4).

The modern F¹⁴C CO₂ signature in Shallow 1 forest boreholes (Fig. 3c) suggests a year-round dominant source of CO₂ from
root respiration and the decomposition of very recently fixed soil organic matter. As the root systems are deeper and more
developed in the forest soils, there is a higher input of modern carbon compared to the meadows. The soils in the forested area
410 are shallow (in some areas < 10 cm deep) and are dominated by large pebbles and fragments of the carbonate bedrock and
shallow roots. Thus, shallow depth carbon sequestration may be suppressed in the forest soil, resulting in a CO₂ profile
dominated by deeper root respiration (Hasenmueller et al., 2017; Tune et al., 2020).

5.2 Sources and variability of CO₂ at 5 m depth

415 CO₂ concentrations at 5 m depth vary considerably over the sampling period and between individual sites (Fig. 5a). CO₂
concentrations are generally higher in the forest boreholes (Deep 1, Deep 2) than in the meadow boreholes (Deep 3, Deep 4),
likely due to the high volumes of CO₂ produced by autotrophic respiration of the mature woodland root system which
penetrates deep into the epikarst. The significant negative correlation between pCO₂ and MMT is highly influenced by borehole



Deep 1, where very high CO₂ concentrations were measured in June 2022 and June 2023 (Fig. 5b). The CO₂ δ¹³C values across
420 all boreholes reflects the isotopic value of the C3 dominated ecosystem of the catchment, and does not indicate any C4 plant
input from the nearby fields. Notably, the ecosystem composition of the overlying vegetation (meadow vs. forest) influences
the isotopic composition of CO₂ at 5 m in the same way as the shallow boreholes, with a slightly lower δ¹³C in the meadow
than the forest. The F¹⁴C values of epikarst CO₂ vary across all deep boreholes by ± 0.02 around a mean value of 1.00 (Fig.
5c) suggesting that the F¹⁴C composition of CO₂ occurring in the shallower soil zone is from modern tree root CO₂ production
425 (Breecker et al., 2012; Tune et al., 2020). Furthermore, the year-round modern CO₂ F¹⁴C values in the deeper meadow
boreholes Deep 3 and Deep 4 compared to the seasonally pronounced signal in the shallower boreholes of Shallow 2, highlights
the potential influence of the meadow doline morphology. Boreholes Deep 3 and Deep 4 were drilled on the edge of the doline
beneath shallow leptosols like those found in the forest, while Shallow 2 was drilled fully within the doline. Unfortunately,
there is no epikarst depth borehole installed within the lower basin of the meadow to verify whether the seasonal signal
430 measured at Shallow 2 translates to the deeper subsurface.

Whilst many studies point to the degradation of exported aged organic matter being the main source of karstic ground air
(Breecker et al., 2012; Matthey et al., 2016; Bergel et al., 2017), epikarst CO₂ in the Milandre cave catchment has predominantly
modern F¹⁴C values, and does not show seasonal isotopic variability. This suggests that the majority of the CO₂ at 5 m is likely
435 supplied by contemporaneous C3 tree root respiration. This also excludes the contribution of substantial amounts of decadal-
aged soil material containing bomb spike carbon due the enrichment in ¹⁴C by thermonuclear weapons testing during 1950's
and 1960's (Trumbore, 2000; Shi et al 2020). This result supports the body of literature stating that, in addition to the export
and respiration of older carbon, large volumes of modern carbon are also transported into the unsaturated zone, likely in large
part through deep root respiration (Breecker et al., 2012; Campeau et al., 2019; Tune et al., 2020). This suggests that deep
440 roots, as found in mature forest ecosystems, might be more important than previously thought in contributing to the ground air
budget.

5.3 Ventilation driven isotopic variation in cave air

The CO₂ dynamics in the cave show distinct variations in concentrations and isotopic compositions between the two sampling
points Upstream and Downstream (Fig. 6a, b, c). Cave ventilation dynamics modulate the mixing ratio between the atmosphere
and the other contributing pools, and are usually the dominant source of variability (Kukuljan et al., 2021; Buzjak et al., 2024).
445 Recent modelling of air flow dynamics in Milandre cave found that outside temperature controls 95 % of flow variability
(Garagnon et al., 2022). During colder months when the outside temperature is ≤ 8 °C, the air in the cave flows topographically
upwards from the northern downstream entrance close to the Downstream site, to the higher entrance closer to Upstream.
When the temperature increases above 8 °C, the ventilation regime reverses. This seasonality is reflected in the alternating
450 concentrations and isotopic composition of the CO₂ at the cave sampling sites as they experience varying amounts of dilution
from atmospheric air during the year. CO₂ degassing of the cave river at Upstream reduces the dilution effect in the upper



455 passage. The effects of ventilation can also be observed in the higher spatial resolution sampling during the cross trip (Fig. 8a, b, c) whereby the summer regime ventilation resulted in lower concentrations, more positive $\delta^{13}\text{C}$, and increased $F^{14}\text{C}$ due to atmospheric mixing closer to the upper entrance (Upstream site). Spatially, a marked decrease in CO_2 concentration and $F^{14}\text{C}$ occurs at sampling location 10 and 11 (~750 to 1000 m) from the cave entrance respectively, though little change is observed in the $\delta^{13}\text{C}$. This air input could be associated with an older organic matter pool which, however, contributes only little to the entire CO_2 mass flux.

5.4 Sources and variability of CO_2 in cave air

460 The Keeling plot y-intercepts show that the composition of the gas pool (karst endmember) that mixes with atmospheric air in the cave changes seasonally (Fig. 7c). It is important to note that, while the isotopic composition of cave CO_2 is influenced by ventilation-driven dynamics, the Keeling plot y-intercept represents the composition of the subsurface gas that mixes with the atmospheric air during ventilation and is not affected by it. The $\delta^{13}\text{C}$ of the karst endmember is mostly stable, varying -26‰ , $\pm 2\text{‰}$, a value typically associated with the CO_2 produced by the C3 plants which dominate the catchment ecosystem. This
465 value is also very similar to the $\delta^{13}\text{C}$ CO_2 values of soil and epikarst gas and reinforces the notion of a common source. Previous work investigating aquifer dynamics using ^{222}Rn at Milandre suggested that the majority of the cave CO_2 comes from the overlying soils (Savoy et al., 2011). The $F^{14}\text{C}$ on the other hand shows seasonal variability with distinctly more “modern” (closer to $F^{14}\text{C} = 1$) during the summer and “aged” ($F^{14}\text{C} < 1$) CO_2 during the winter. The transition from an $F^{14}\text{C}$ of 0.94 to 0.88 represents a change in the mean apparent age of CO_2 from ~ 100 to 1000 yrs, well beyond the assumed residence time of
470 water in the epikarst of ~ 5.5 to 6.6 years (Affolter et al., 2020).

Several mechanisms may be responsible for the seasonal $F^{14}\text{C}$ fluctuations of the endmember. Varying contributions of host rock-derived carbon to cave air through shifts in the host rock dissolution regime could affect the isotopic composition of cave air. Dissolution of the host rock carbonate can occur under a wide range of conditions between two extreme cases: in a
475 completely closed system, the aqueous solution becomes isolated from the soil CO_2 reservoir after passing into the epikarst resulting in a theoretical 50:50 contribution ratio of carbon ions in solution from the carbonate host rock and from soil air, and overall decreasing $F^{14}\text{C}$ to as low as 0.5 (Fohlmeister et al., 2011; Milanolo & Gabrovšek, 2015). On the other hand, in a completely open system the aqueous solution can continuously exchange with an unlimited soil CO_2 reservoir resulting in most carbon atoms sourced from the soil CO_2 reservoir, and the rock contribution being minimal (Fohlmeister et al., 2011).
480 Most natural systems exist in an intermediate state between fully open and fully closed settings.

If the seasonal variability in CO_2 $F^{14}\text{C}$ in Milandre cave reflected seasonal shifts in the “openness” of the system, summers (with higher $F^{14}\text{C}$) would be characterised by a more open system with higher rates of exchange between the aqueous solution and the soil CO_2 reservoir. The observed shift to lower $F^{14}\text{C}$ in winter would reflect a more closed system with a higher
485 contribution of the $F^{14}\text{C}$ free carbonate bedrock. Shifts in the open-closed continuum would likely result in changes in the $\delta^{13}\text{C}$

of the endmember (Fairchild & Baker, 2012) which is not seen in the cave air, with an expected lower $\delta^{13}\text{C}$ in a more open system, and an increase in a more closed system because of the higher solid host rock carbon contribution ($\delta^{13}\text{C} \approx 0 \text{ ‰}$). However, varying amounts of isotopic fractionation can occur when CO_2 is degassed from the drip water DIC pool into the cave atmosphere, potentially influencing the isotopic composition of the measured cave air CO_2 (Mickler et al., 2019).

490

We constructed a mixing model which allows us to evaluate how much variability in the Keeling plot y-intercept (i.e. the second source of carbon to cave air besides the atmosphere) can be explained by variation in DIC contribution from dissolution regime changes and degassing fractionation. This model assumes that the Keeling plot y-intercept is itself a mixture of two endmembers that contribute CO_2 to cave air, the modern soil ($F^{14}\text{C}_{\text{soil}} = 1$), and the DIC ($F^{14}\text{C}_{\text{DIC}}$), where the $F^{14}\text{C}_{\text{DIC}}$ itself represents a mixture of dissolved soil CO_2 and DIC from carbonate mineral dissolution that is degassed into the cave air. The $F^{14}\text{C}$ soil represents direct input of CO_2 soil gas into the cave.

495

The mixing ratio between $F^{14}\text{C}_{\text{soil}}$ and $F^{14}\text{C}_{\text{DIC}}$ results in the $F^{14}\text{C}$ of CO_2 entering the cave atmosphere ($F^{14}\text{C}_{\text{cave}}$). Thus, the cave air CO_2 $F^{14}\text{C}$ can be expressed as (where f is fraction, defined as between 0 and 1):

500

$$F^{14}\text{C}_{\text{cave}} = f_{\text{soil}}F^{14}\text{C}_{\text{soil}} + f_{\text{DIC}}F^{14}\text{C}_{\text{DIC}} \quad (3)$$

Solve for f_{soil} and f_{DIC} , where $f_{\text{DIC}} = 1 - f_{\text{soil}}$:

505

$$F^{14}\text{C}_{\text{cave}} = f_{\text{soil}}F^{14}\text{C}_{\text{soil}} + (1 - f_{\text{soil}})F^{14}\text{C}_{\text{DIC}} \quad (4)$$

For $F^{14}\text{C}$, fractionation is generally negligible during carbonate dissolution and degassing compared to $\delta^{13}\text{C}$, due to measurement precision i.e. % vs ‰ (Fohlmeister et al., 2011). We use the mixing calculation (Eq. 4) to estimate the contributions of f_{soil} and f_{DIC} using the highest (0.94), an intermediate (0.90), and the lowest (0.88) measured cave CO_2 $F^{14}\text{C}$ values ($F^{14}\text{C}_{\text{cave}}$), and $F^{14}\text{C}$ DIC ($F^{14}\text{C}_{\text{DIC}}$) based on the highest (0.98) intermediate (0.88) and lowest (0.78) measured values of drip water DIC. We find that when $F^{14}\text{C}_{\text{DIC}} = 0.98$, the mixing model results in impossible scenarios with $f_{\text{soil}} > 1$ and $f_{\text{DIC}} < 0$ because this value is higher than the highest $F^{14}\text{C}_{\text{cave}}$, and a highly unlikely scenario based on our observations and the literature where $f_{\text{soil}} = 0$ and $f_{\text{DIC}} = 1$ when $F^{14}\text{C}_{\text{DIC}} = 0.88$, as this corresponds to the lowest $F^{14}\text{C}_{\text{cave}}$ value (Fig. 9a). Only the scenario with lowest $F^{14}\text{C}_{\text{DIC}} = 0.78$ produced realistic mixing fractions. Overall, this implies that there is a discrepancy between the measured $F^{14}\text{C}_{\text{DIC}}$ and what is derived by a simplified mixing model based on the $F^{14}\text{C}$ of cave CO_2 , with $F^{14}\text{C}_{\text{DIC}}$ values too high to result in the $F^{14}\text{C}_{\text{cave}}$ composition that we observe. Thus, carbonate dissolution and subsequent degassing of CO_2 from drip water DIC to cave air is unlikely to be the dominant process explaining the shifts in cave air $F^{14}\text{C}$ over time.

515



The $F^{14}C_{DIC}$ is based on the analysis of 9 drip water sites of varying drip rates and ecosystem coverage. It is possible that the
520 sampling set up did not capture the true range of $F^{14}C_{DIC}$ in the drip water, though rather unlikely due to the diversity in drip
rate and hydrological response of drips measured.

As our mixing ratios derived from measured DIC values are mostly not possible according to the two endmember mixing
scenario, we then explored how a wider theoretical range of $F^{14}C_{DIC}$ values (from closed to mainly open system dissolution
525 conditions, 0.50 to 0.90 $F^{14}C$) would affect the contributing fractions of f_{soil} and f_{DIC} . Variations in $F^{14}C_{DIC}$: 0.50 to 0.85
result in viable mixing fractions across the range of $F^{14}C_{cave}$, with the f_{soil} (20 to 76 %) and f_{DIC} (24 to 80 %) differing
widely (Fig. 9b).

As the average value of cave CO_2 $\delta^{13}C$ is -26 ‰ (we take a range from -25 to -27 ‰), we created a similar two-endmember
530 mixing calculation for $\delta^{13}C$ values to test whether the mixing ratios derived from $F^{14}C$ translate to observed $\delta^{13}C$ values. For
this we used the average $\delta^{13}C$ of soil CO_2 ($\delta^{13}C_{soil}$) = -26 ‰, and the $\delta^{13}C$ of the DIC ($\delta^{13}C_{DIC}$) = -15 ‰ (estimated from an
average of the $\delta^{13}C$ produced during the $F^{14}C$ DIC AMS measurement (see Appendix B)).

Fractionation effects during degassing must be considered when modelling $\delta^{13}C$. If equilibrium fractionation between DIC and
535 $CO_{2(g)}$ occurs, the fractionation factor ($\Delta^{13}C_{HCO_3-CO_2,eq}$) at 10.5 °C between HCO_3^- and CO_2 is 9.54 ‰, with the gas being
9.54 ‰ depleted in ^{13}C relative to the fluid (Mook et al., 1974). Kinetic fractionation can occur during rapid degassing of CO_2
as well as during rapid precipitation of carbonate minerals (Mickler et al., 2019). If kinetic fractionation occurs during
degassing, this results in a greater depletion of the dissolved CO_2 in ^{13}C compared to equilibrium fractionation (i.e. a more
positive $\delta^{13}C_{DIC}$). The possible ranges reported for the composition of CO_2 generated from kinetic fractionation during
540 degassing in caves vary widely, with some reporting $\Delta^{13}C_{HCO_3-CO_2,kin}$ close to that resulting from equilibrium fractionation
(Dulinski & Rozanski et al., 1990), and others a range of 10 to 65 ‰ (Mickler et al., 2019). The extent of kinetic fractionation
is expected to depend on the amount of degassing that occurs, which is a function of the disequilibrium between the fluid and
the surrounding air (Frisia et al., 2011). In our system with limited geochemical data regarding fluid compositions, it is difficult
to determine what extent of kinetic fractionation may have occurred. Hence, we first assume that the fractionation is < -9.54
545 ‰ (i.e., greater compared to equilibrium conditions) and take a moderate but arbitrary value ballpark of $\Delta^{13}C_{HCO_3-CO_2,kin}$ =
30 ‰.

A mixing calculation is then applied to assess if the measured range of the karst endmember $\delta^{13}CO_2$ given by the Keeling plot
can be consistent with the extended range of $F^{14}C_{DIC}$ and measured $F^{14}C_{cave}$ under conditions with equilibrium degassing and
550 kinetic degassing:



Equilibrium degassing:

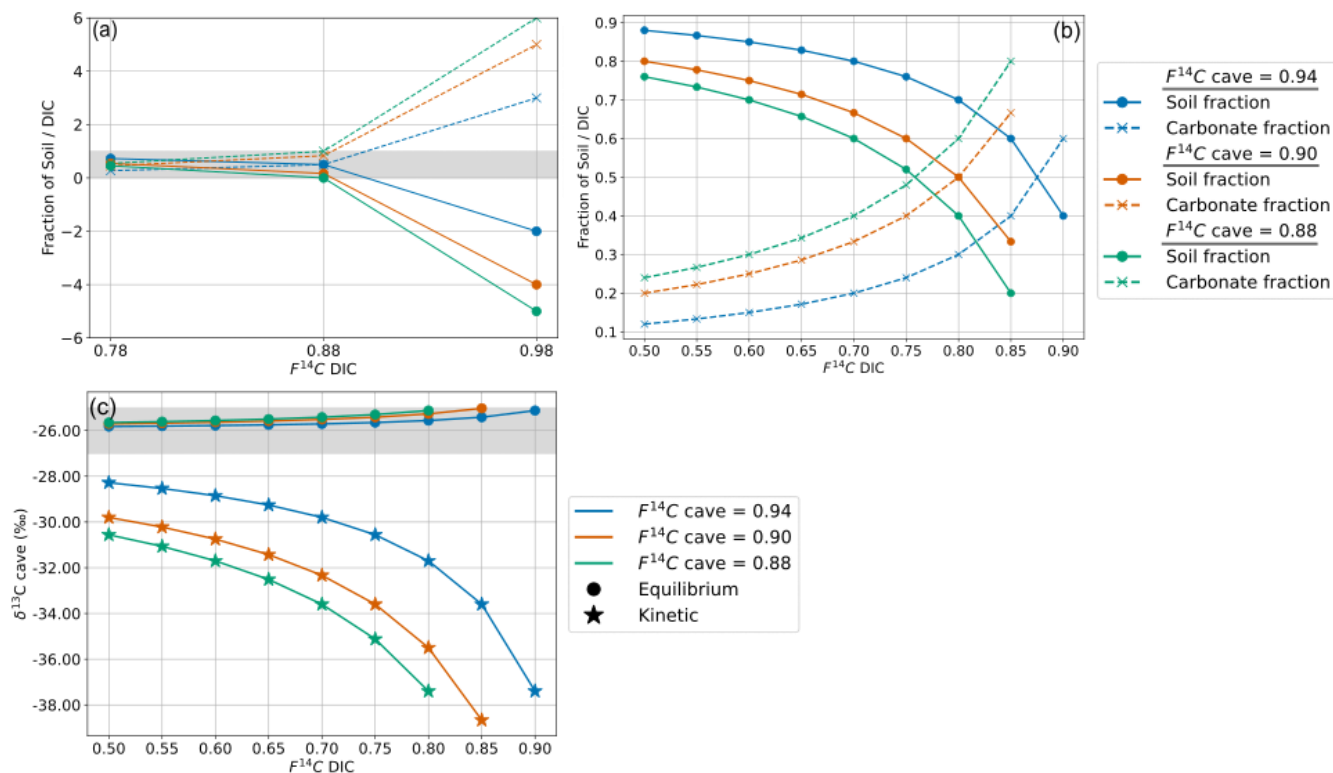
$$\delta^{13}C_{cave} = f_{soil}\delta^{13}C_{soil} + f_{DIC}(\delta^{13}C_{DIC} - \Delta^{13}C_{HCO_3-CO_2,eq}) \quad (5)$$

555 Kinetic degassing:

$$\delta^{13}C_{cave} = f_{soil}\delta^{13}C_{soil} + f_{DIC}(\delta^{13}C_{DIC} - \Delta^{13}C_{HCO_3-CO_2,kin}) \quad (6)$$

For the maximum (0.94), intermediate (0.90), and minimum (0.88) values of the endmember $F^{14}C$, only equilibrium fractionation during degassing can explain the observed $\delta^{13}C_{cave}$ value of approximately -26 ‰ (Fig. 9c). Kinetic fractionation scenarios result in very negative $\delta^{13}C_{cave}$ values which do not fit those measured, except when using very small kinetic fractionation factors similar to that of the equilibrium fractionation ($\Delta^{13}C_{HCO_3-CO_2,kin}$ of -10 ‰, see Appendix C). It is possible that kinetic fractionation occurs between Milandre cave waters and the cave air due to atmospheric ventilation which occurs year-round. The fresh atmospheric air which enters from the upper entrance in the summer and the lower entrance in the winter creates a concentration gradient between the CO_2 present within cave waters and the concentration in the cave atmosphere.

560
565 However, the rapidly increasing pCO_2 with distance from the cave entrance (Fig. 8a) implies that the concentration gradients required for kinetic fractionation do not occur throughout most of the cave passage and that kinetic influences are probably minimal.



570 **Figure 9. a) Mixing model between f_{soil} and f_{DIC} for the measured range of $F^{14}C_{DIC}$ values and $F^{14}C_{cave}$ values of 0.94 (blue), 0.9 (orange) 0.88 (green). The grey bar shows physically possible mixing ratios between 0 and 1. b) Mixing model between f_{soil} and f_{DIC} using the extended DIC $F^{14}C$ range and cave air $F^{14}C$ values. c) Cave air $\delta^{13}C$ for varying DIC $F^{14}C$ and cave air $F^{14}C$ values with equilibrium fractionation at -9.54 ‰ (circles) and kinetic fractionation at -30 ‰ (stars). The grey bar shows cave air $\delta^{13}C$ range which fits the measured values between -25 ‰ and -27 ‰.**

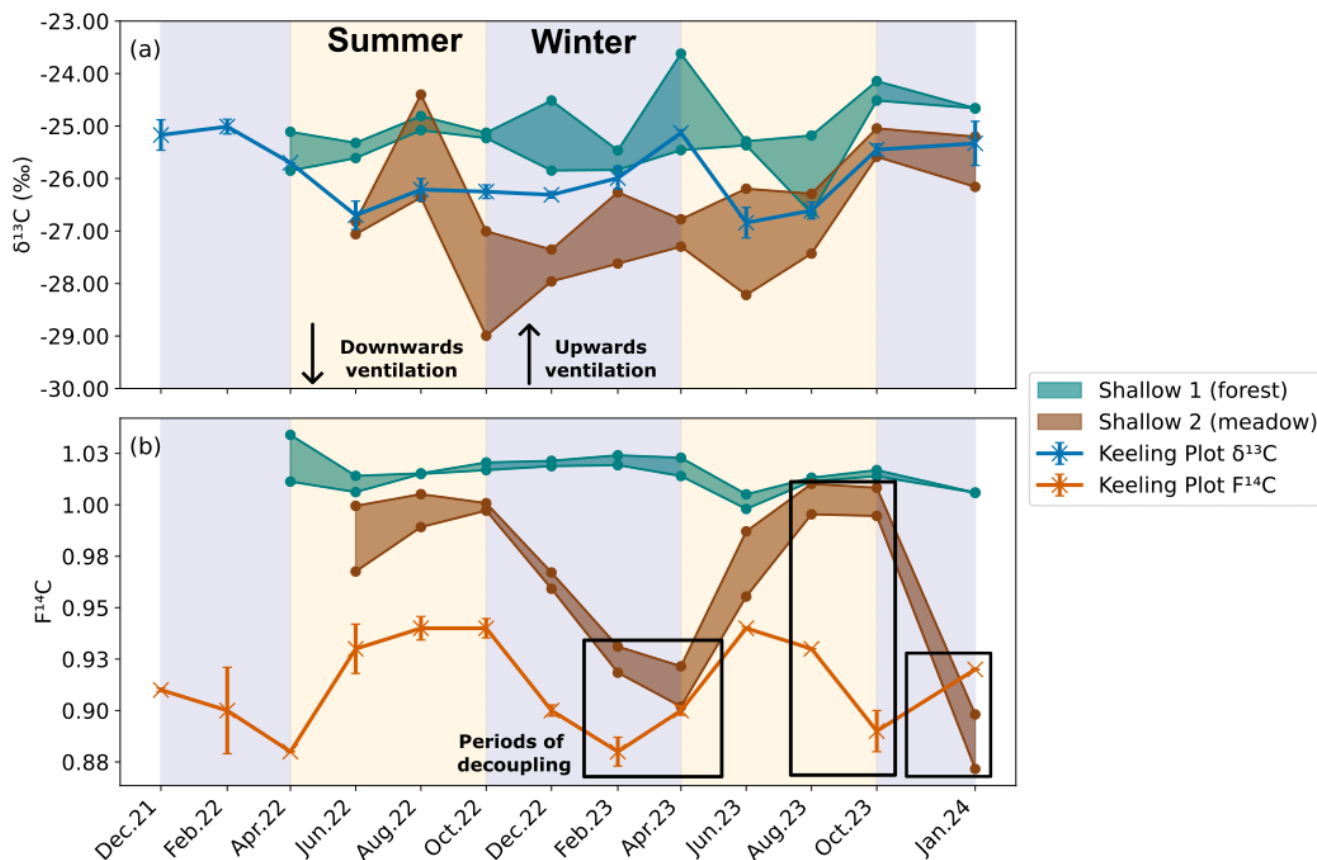
575

Overall, the $F^{14}C_{DIC}$ measured beyond $F^{14}C = 0.90$ is too high to reproduce our measured cave air CO_2 $F^{14}C$ and $\delta^{13}C$. We measured the $F^{14}C_{DIC}$ in drips covering diverse locations, drip rates, and coverage so it is unlikely that our DIC data is not representative of the system. The $F^{14}C_{DIC}$ of the cave river was not measured, however previous studies on the Milandre cave river have suggested that in non-flooding conditions, the river is fed by slow diffuse flow as the epikarst acts as a buffer, storing water and dampening the signal of normal rainfall. During flooding events, the epikarst aquifer is bypassed and the stream is mainly fed by fresh fracture flow (Perrin et al., 2003; Savoy et al., 2011). A diffuse flow fed river is likely to have isotopic characteristics similar to that of the drip waters, which have higher $F^{14}C$ suggesting more open system dissolution conditions. In contrast, times of flooding and soil saturation results in less exchange with the soil gas reservoir, leading to dissolution under more closed conditions (Perrin et al., 2003; Savoy et al., 2011). However, the drip water $F^{14}C_{DIC}$ is relatively stable over one year of monitoring in a variety of hydrological conditions, implying that variations in host rock dissolution and degassing dynamics are not the explanation for the variation in $F^{14}C$ and $\delta^{13}C$ of the endmember.

585



The meadow soil boreholes in the doline (Shallow 2) have similar patterns in CO₂ composition to the endmember, with a δ¹³C of -26 ‰ and variable F¹⁴C (Fig. 10a & b). In 2022, the F¹⁴C in the meadow soil and karst endmember align closely, but this
590 decouples slightly in 2023 during the transitional periods between winter and spring where the karst endmember F¹⁴C changes before the meadow. This suggests that, instead of the soils influencing the cave air due to seasonal changes in soil respiration, the cave ventilation regime could be influencing the soil F¹⁴C. The cave ventilates upwards in winter from Downstream to Upstream in a chimney effect (and vice versa in summer). Here, the lower F¹⁴C karst endmember CO₂ may flow upwards through the highly fractured epikarst of the doline and ventilate the meadow soils, resulting in a mixture of low F¹⁴C CO₂ from
595 the karst endmember and modern CO₂ from the soils. This possibly reflects a contribution of older CO₂ from within the karst itself, likely from a “ground air” reservoir of older respiring organic material in the epikarst as found by several other studies (Breecker et al., 2012; Noroha et al., 2015; Matthey et al., 2016; Bergel et al., 2017). There are likely several reservoirs of older organic material throughout the downstream catchment of Milandre which may contribute the low F¹⁴C CO₂ to the ventilating cave air in winter. In summer the ventilation reverses, and the higher F¹⁴C CO₂ from the soil is transported downwards into the
600 cave, increasing the F¹⁴C of the cave endmember CO₂. The F¹⁴C of the karst endmember is always lower than the meadow soil F¹⁴C, implying that there is always mixing between the soils and the karst endmember. Similar upwards transport of CO₂ in karst boreholes has been observed in Nerja Cave, Spain (Benavente et al., 2010; Benavente et al., 2015), and in the Gibraltar karst (Matthey et al., 2016). We do not observe significant effects of the winter upwards ventilation in the F¹⁴C CO₂ in any of the deeper boreholes in the meadow or any of the boreholes in the forest. This could be related to the location of Shallow 2 in
605 the doline, whilst the rest of the boreholes are situated higher on the banks (Deep 3 and Deep 4), or further away from the doline in the forest (Deep 1 and Deep 2). The topography likely reflects influences of the secondary porosity in the bedrock, which is possibly more highly fractured in the meadow doline formation compared to the forest leading to a greater effect of ventilation in the meadow area and an undisturbed modern ¹⁴C signature of forest soils. As the doline structure likely has a higher secondary porosity and is more highly fractured than the higher bedrock, ventilation effects may be more important
610 here than at the other locations.



615

Figure 10. Comparison between the a) $\delta^{13}\text{C}$ and b) F^{14}C of the shallow depth boreholes in the forest (Shallow 1, green) and meadow (Shallow 2, brown), and the Keeling plot endmembers $\delta^{13}\text{C}$ (blue) and F^{14}C (orange) also show in Figure 7. Summer (yellow) and winter (blue) seasons are highlighted by the coloured background. The direction of cave ventilation is shown by the arrows with downwards ventilation (from Upstream to Downstream) in summer, and upwards ventilation (Downstream to Upstream). Periods of decoupling between the F^{14}C of the meadow borehole and the cave endmember are shown in black boxes.

620

The accumulation of the older organic carbon in the epikarst likely occurs over time. Soil layers in karst regions often accumulate on bedrock with deep vertical fractures (Cheng et al., 2023). This decreases the ability of long-term storage of older soil carbon pools due to preferential fracture flow, also known as subsurface leakage, which destabilises the oldest soil layer and leads to export of older carbon into the epikarst (Sánchez-Cañete et al., 2018; Wan et al., 2018). Several studies have acknowledged this potential source of CO_2 produced autochthonously inside the epikarst by the microbial degradation of this old soil, plant, or root material which was previously washed into the unsaturated zone, contributing older CO_2 to the ground air mix (Noronha et al., 2015; Bergel et al., 2017; Ding et al., 2023).

625



6 Conclusion

630 We conducted a comprehensive investigation over two years into the dynamics of CO₂ concentrations, δ¹³C and F¹⁴C
composition across different land covers and soil types within the Critical Zone at Milandre cave in northern Switzerland. Our
analysis found distinct seasonal fluctuations in CO₂ levels in soil boreholes in both forest and meadow areas, with higher
concentrations during summer compared to winter. Low δ¹³C values of ~ -26 ‰ indicate respiration of C₃ plants which
dominate the catchment area. The stable modern F¹⁴C of ~ 1.00 in shallow forest boreholes indicated a year-round modern
635 CO₂ contribution from tree and plant roots to the subsurface, consistent with a well-ventilated soil. On the other hand, samples
from meadow boreholes situated in a doline with a thick, well developed soil cover displayed seasonality in F¹⁴C from ~ 0.88
in the winter and spring to ~ 1.00 in summer.

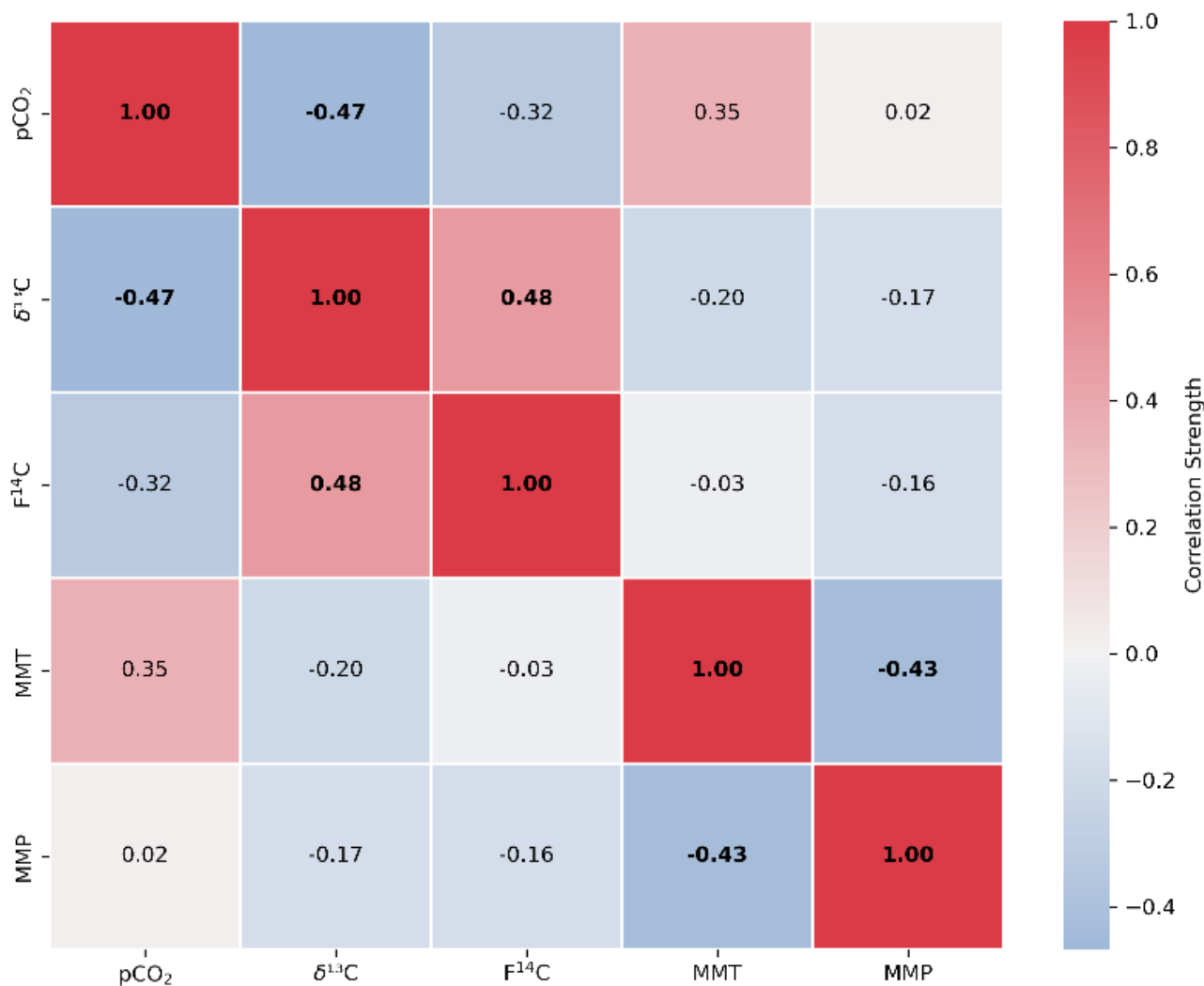
In the epikarst we observed substantial variability in CO₂ concentrations across the catchment (~ 3000 to ~ 37'000 ppmV),
640 with higher concentrations in boreholes with forest cover than those with meadow cover. Despite differences in surface
vegetation, the isotopic compositions of δ¹³C and F¹⁴C remained stable in both forest and meadow environments, reflecting
the dominant modern C₃ vegetation signature contributing to the ground air. The year-round modern epikarst CO₂ in meadow
boreholes Deep 3 and Deep 4, in contrast to the seasonally attenuated signal in the thicker meadow soils.

645 Large variations in cave air CO₂ concentrations (atmospheric to ~ 30'000 ppmV), δ¹³C (~ -9 to -25 ‰), and F¹⁴C (0.88 to
0.98), are controlled by direction changes in the seasonal temperature driven cave ventilation regime. The seasonal changes in
the isotopic composition of the Keeling plot derived karst endmember cannot be explained with the observed DIC F¹⁴C range,
suggesting that bedrock dissolution and degassing dynamics are likely not the cause of the isotopic variation in the cave air.
The isotopic characteristics of the cave air are comparable to those of the meadow doline soil. The karst endmember CO₂ F¹⁴C
650 changes before the soil in times of variation, and is always older. This suggests that the cave ventilation contributes older CO₂
to the doline soils, likely sourced from a reservoir of aged organic material in the epikarst, during the upward winter ventilation
regime. In summer, the reversed downwards ventilation contributes younger soil CO₂ to the cave, mixing with the older
epikarst reservoir. The consistently low δ¹³C signature of the karst endmember implies that the impact of carbonate dissolution
on the system is low, and that the CO₂ is contributed from either modern soils or aged organic material in the epikarst.

655
Our study provides important insights into how carbon is transported to the subsurface in karstic Critical Zones. Understanding
these processes is crucial for accurate estimation of the size of subsurface CO₂ pools (ground air), and to refine terrestrial CO₂
budgets. Moving forward, it would be beneficial for future research to undertake more detailed investigation of CO₂ transport
into the subsurface implementing ¹⁴C analysis to further constrain the sources of ground air. Furthermore, higher resolution
660 monitoring over periods of interest, could assist us in understanding short-term variations.



Appendix A



665 A1 Spearman's rank correlation matrix displaying the Spearman's rho of CO₂ concentration, δ¹³C and F¹⁴C, Mean Monthly
Temperature (MMT) and Mean Monthly Precipitation (MMP) from Fahy weather station from samples from soil depth boreholes
Shallow 1. Parameters with a significant correlation (positive or negative) are bolded and the strength of the correlation is indicated
by the blue – red colour bar.

670



675 A2 Spearman's rank correlation matrix displaying the Spearman's rho of CO₂ concentration, δ¹³C and F¹⁴C, Mean Monthly Temperature (MMT) and Mean Monthly Precipitation (MMP) from Fahy weather station from samples from soil depth borehole Shallow 2. Parameters with a significant correlation (positive or negative) are bolded and the strength of the correlation is indicated by the blue – red colour bar.



680 A3 Spearman's rank correlation matrix displaying the Spearman's rho of CO₂ concentration, δ¹³C and F¹⁴C, Mean Monthly Temperature (MMT) and Mean Monthly Precipitation (MMP) from Fahy weather station from samples from epikarst depth boreholes Deep 1 and Deep 2. Parameters with a significant correlation (positive or negative) are bolded and the strength of the correlation is indicated by the blue – red colour bar.



685 **A4 Spearman's rank correlation matrix displaying the Spearman's rho of CO₂ concentration, δ¹³C and F¹⁴C, Mean Monthly Temperature (MMT) and Mean Monthly Precipitation (MMP) from Fahy weather station from samples from epikarst depth boreholes Deep 3 and Deep 4. Parameters with a significant correlation (positive or negative) are bolded and the strength of the correlation is indicated by the blue – red colour bar.**

690



695 A5 Spearman's rank correlation matrix displaying the Spearman's rho of CO₂ concentration, δ¹³C and F¹⁴C, Mean Monthly Temperature (MMT) and Mean Monthly Precipitation (MMP) from Fahy weather station from samples from the Downstream cave site. Parameters with a significant correlation (positive or negative) are bolded and the strength of the correlation is indicated by the blue – red colour bar



700 A6 Spearman's rank correlation matrix displaying the Spearman's rho of CO₂ concentration, δ¹³C and F¹⁴C, Mean Monthly Temperature (MMT) and Mean Monthly Precipitation (MMP) from Fahy weather station from samples from the Upstream cave stie. Parameters with a significant correlation (positive or negative) are bolded and the strength of the correlation is indicated by the blue – red colour bar.

705

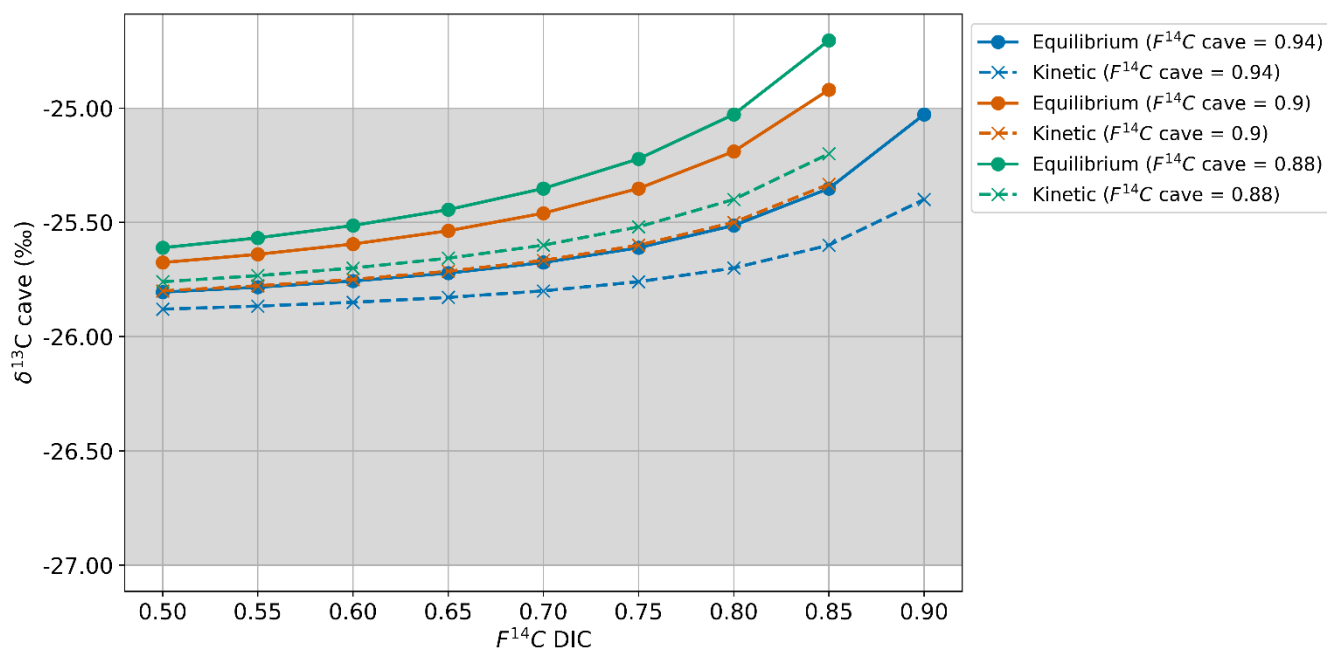


710 **B1 Drip water dissolved inorganic carbon F¹⁴C and AMS derived δ¹³C from the actively dripping galleries nearby Upstream and Downstream.**

Drip	Sampling date	F ¹⁴ C	F ¹⁴ C % error	AMS δ ¹³ C (‰)
GF1	Dec.21	0.86	0.92	-13.6
GF2	Dec.21	0.94	0.91	-14.3
GR2	Dec.21	0.91	0.92	-12.4
GR3	Dec.21	0.98	0.93	-13.5
GR4	Dec.21	0.91	0.97	-14.7
GR5	Dec.21	0.90	0.97	-14.2
GR6	Dec.21	0.85	1.02	-13.6
GF1	Feb.22	0.87	0.99	-12.6
GF3	Feb.22	0.95	0.96	-12.7
GR3	Feb.22	0.90	0.97	-14.1
GR4	Feb.22	0.89	0.99	-12.7
GR6	Feb.22	0.84	1.00	-11.9
GR6	Feb.22	0.88	0.99	-10.6
GF1	Apr.22	0.88	0.93	-12.8
GF2	Apr.22	0.93	0.89	-11.6
GF3	Apr.22	0.98	0.86	-12.1
GR1	Apr.22	0.87	0.90	-12.6
GR2	Apr.22	0.89	0.92	-12.1
GR3	Apr.22	0.90	0.93	-12.2
GR4	Apr.22	0.90	0.93	-13.4
GR5	Apr.22	0.89	0.98	-13.7
GR6	Apr.22	0.90	0.99	-13.6
GF1	Jun.22	0.87	1.11	-18.0
GF2	Jun.22	0.93	1.11	-18.9
GF3	Jun.22	0.96	1.07	-18.6
GR1	Jun.22	0.88	1.12	-17.4
GR2	Jun.22	0.93	1.09	-17.6
GR3	Jun.22	0.89	1.12	-17.9
GR4	Jun.22	0.89	1.12	-18.9
GR5	Jun.22	0.90	1.11	-17.9
GR6	Jun.22	0.92	1.12	-19.0
GF1	Aug.22	0.86	1.10	-17.1
GF2	Aug.22	0.92	1.12	-19.8
GR1	Aug.22	0.87	1.03	-8.9



GR2	Aug.22	0.91	1.09	-18.3
GR4	Aug.22	0.93	1.10	-19.2
GR5	Aug.22	0.91	1.10	-19.5
GR6	Aug.22	0.93	1.11	-20.8
GF1	Oct.22	0.84	1.05	-9.4
GF2	Oct.22	0.94	1.12	-20.3
GF3	Oct.22	0.95	1.11	-20.8
GR1	Oct.22	0.86	1.14	-17.2
GR2	Oct.22	0.88	1.14	-22.6
GR4	Oct.22	0.91	1.13	-18.7
GR5	Oct.22	0.89	1.13	-18.3
GR6	Oct.22	0.91	1.11	-19.1
GF1	Dec.22	0.86	1.01	-14.1
GF2	Dec.22	0.88	0.94	-14.1
GF3	Dec.22	0.94	0.95	-11.1
GR1	Dec.22	0.86	1.00	-11.5
GR4	Dec.22	0.89	0.98	-11.5
GR5	Dec.22	0.89	1.01	-12.6
GR6	Dec.22	0.78	1.02	-12.9



C1 Cave air $\delta^{13}\text{C}$ for varying DIC $F^{14}\text{C}$ and cave air $F^{14}\text{C}$ values with equilibrium fractionation at -9.54 ‰ (solid lines) and kinetic fractionation at -10 ‰ (dashed lines).

720

Code and data availability

The data, code for Spearman's rank statistics, and code to reproduce the model results are publicly available on Zenodo at <https://doi.org/10.5281/zenodo.14253707>.

Author contributions

725 Sarah Rowan: Conceptualization, Formal analysis, Investigation, Methodology, Visualization, Software, Writing – original draft preparation.

Marc Luetscher: Conceptualization, Resources, Visualization, Writing – review & editing.

Thomas Laemmel: Methodology, Validation, Writing – review & editing.

Anna Harris: Methodology, Writing – review & editing.

730 Sönke Szidat: Writing – review & editing.

Franziska Lechleitner: Conceptualization, Funding acquisition, Project administration, Resources, Supervision, Writing – review & editing.



Competing interests

The authors declare that they have no conflict of interest.

735 Disclaimer

Acknowledgements

This work was supported by the Swiss National Science Foundation Ambizione grant number 186135. We gratefully thank the staff of the Swiss Institute of Speleology and Karst Studies for their previous and continued work in Milandre cave, and
740 for their contribution of field assistance and expertise in karst science. Special thanks to Claudio Pastore for his assistance during the cross trip. We express our gratitude to the Spéléo Club Jura for the initial exploration of Milandre cave, and for their persistent work and maintenance of the area. We also appreciate Daniel Pape, for continued access to the cave entrance and boreholes. Thank you also to Madalina Jaggi, Dr. Oliver Kost, and Prof. Heather Stoll for providing access and support using the Picarro system. Graphitizations and AMS measurements were also assisted by Michael Staub and Dr. Gary Salazar.
745 Generative AI (ChatGPT versions 3.5, 4 and 4o) was used for code troubleshooting.

References

- Affolter, S., Steinmann, P., Aemisegger, F., Purtschert, R., & Leuenberger, M. (2020). Origin and percolation times of Milandre Cave drip water determined by tritium time series and beryllium-7 data from Switzerland. *Journal of Environmental Radioactivity*, 222, 106346. <https://doi.org/10.1016/j.jenvrad.2020.106346>
750
- Atkinson, T. C. (1977). Carbon dioxide in the atmosphere of the unsaturated zone: An important control of groundwater hardness in limestones. *Journal of Hydrology*, 35(1), 111–123. [https://doi.org/10.1016/0022-1694\(77\)90080-4](https://doi.org/10.1016/0022-1694(77)90080-4)
- Baldini, J. U. L., Bertram, R. A., & Ridley, H. E. (2018). Ground air: A first approximation of the Earth's second largest
755 reservoir of carbon dioxide gas. *Science of The Total Environment*, 616–617, 1007–1013. <https://doi.org/10.1016/j.scitotenv.2017.10.218>
- Benavente, J., Vadillo, I., Carrasco, F., Soler, A., Liñán, C., & Moral, F. (2010). Air Carbon Dioxide Contents in the Vadose Zone of a Mediterranean Karst. *Vadose Zone Journal*, 9(1), 126–136. <https://doi.org/10.2136/vzj2009.0027>
760



- Benavente, J., Vadillo, I., Liñán, C., del Rosal, Y., & Carrasco, F. (2015). Influence of the ventilation of a karst show cave on the surrounding vadose CO₂ reservoir (Nerja, South Spain). *Environmental Earth Sciences*, 74(12), 7731–7740. <https://doi.org/10.1007/s12665-015-4709-8>
- 765 Bergel, S. J., Carlson, P. E., Larson, T. E., Wood, C. T., Johnson, K. R., Banner, J. L., & Breecker, D. O. (2017). Constraining the subsoil carbon source to cave-air CO₂ and speleothem calcite in central Texas. *Geochimica et Cosmochimica Acta*, 217, 112–127. <https://doi.org/10.1016/j.gca.2017.08.017>
- Billings, S., Richter, D., & Yarie, J. (1998). Soil carbon dioxide fluxes and profile concentrations in two boreal forests. *Canadian Journal of Forest Research*, 28. <https://doi.org/10.1139/cjfr-28-12-1773>
- 770 Brantley, S. L., Goldhaber, M. B., & Vala, R. K. (2007). Crossing disciplines and scales to understand the critical zone. *Elements* (Vol. 3, Issue 5, p. 8). <https://doi.org/10.2113/gselements.3.5.307>
- 775 Breecker, D. O. (2017). Atmospheric pCO₂ control on speleothem stable carbon isotope compositions. *Earth and Planetary Science Letters*, 458, 58–68. <https://doi.org/10.1016/j.epsl.2016.10.042>
- Breecker, D. O., Payne, A. E., Quade, J., Banner, J. L., Ball, C. E., Meyer, K. W., & Cowan, B. D. (2012). The sources and sinks of CO₂ in caves under mixed woodland and grassland vegetation. *Geochimica et Cosmochimica Acta*, 96, 230–246. <https://doi.org/10.1016/j.gca.2012.08.023>
- 780 Buzjak, N., Gabrovšek, F., Perşoiu, A., Pennos, C., Paar, D., & Bočić, N. (2024). CO₂ Emission from Caves by Temperature-Driven Air Circulation—Insights from Samograd Cave, Croatia. *Climate*, 12(12), Article 12. <https://doi.org/10.3390/cli12120199>
- 785 Campeau, A., Bishop, K., Amvrosiadi, N., Billett, M. F., Garnett, M. H., Laudon, H., Öquist, M. G., & Wallin, M. B. (2019). Current forest carbon fixation fuels stream CO₂ emissions. *Nature Communications*, 10(1), Article 1. <https://doi.org/10.1038/s41467-019-09922-3>
- 790 Cheng, K., Liu, Z., Xiong, K., He, Q., Li, Y., Cai, L., & Chen, Y. (2023). Migration of Dissolved Organic Matter in the Epikarst Fissured Soil of South China Karst. *Land*, 12(4), Article 4. <https://doi.org/10.3390/land12040887>
- Chiodini, G., Caliro, S., Cardellini, C., Avino, R., Granieri, D., & Schmidt, A. (2008). Carbon isotopic composition of soil CO₂ efflux, a powerful method to discriminate different sources feeding soil CO₂ degassing in volcanic-hydrothermal areas. *Earth and Planetary Science Letters*, 274(3), 372–379. <https://doi.org/10.1016/j.epsl.2008.07.051>



795

Chiti, T., Neubert, R., Janssens, I., Curiel Yuste, J., Sirignano, C., & Certini, G. (2011). Radiocarbon based assessment of soil organic matter contribution to soil respiration in a pine stand of the Campine region, Belgium. *Plant and Soil*, 344, 273–282. <https://doi.org/10.1007/s11104-011-0745-7>

800

Diao, H., Wang, A., Yuan, F., Guan, D., & Wu, J. (2022). Autotrophic respiration modulates the carbon isotope composition of soil respiration in a mixed forest. *Science of The Total Environment*, 807, 150834. <https://doi.org/10.1016/j.scitotenv.2021.150834>

805

Ding, Y., Wang, D., Zhao, G., Chen, S., Sun, T., Sun, H., Wu, C., Li, Y., Yu, Z., Li, Y., & Chen, Z. (2023). The contribution of wetland plant litter to soil carbon pool: Decomposition rates and priming effects. *Environmental Research*, 224, 115575. <https://doi.org/10.1016/j.envres.2023.115575>

810

Dulinski, M., & Rozanski, K. (1990). ‘Formation of $^{13}\text{C}/^{12}\text{C}$ Isotope Ratios in Speleothems: A Semi-Dynamic Model’. *Radiocarbon*, 32(1), 7–16. <https://doi.org/10.1017/S0033822200039904>

Fairchild, I. J., & Baker, A. (2012). *Speleothem Science: From Process to Past Environments*. John Wiley & Sons. <https://doi.org/10.1002/9781444361094.ch5>

815

Fohlmeister, J., Scholz, D., Kromer, B., & Mangini, A. (2011). Modelling carbon isotopes of carbonates in cave drip water. *Geochimica et Cosmochimica Acta*, 75(18), 5219–5228. <https://doi.org/10.1016/j.gca.2011.06.023>

820

Frisia, S., Fairchild, I. J., Fohlmeister, J., Miorandi, R., Spötl, C., & Borsato, A. (2011). Carbon mass-balance modelling and carbon isotope exchange processes in dynamic caves. *Geochimica et Cosmochimica Acta*, 75(2), 380–400. <https://doi.org/10.1016/j.gca.2010.10.021>

Garagnon, J., Luetscher, M., & Weber, E. (2022, July 1). *Ventilation regime in a karstic system (Milandre Cave, Switzerland)*. Conference: 18th International Congress of Speleology, Savoie Mont Blanc.

825

Gigon, R. and Wenger, R. (1986): *Inventaire spe'le'ologique de la Suisse, canton du Jura*. La Chaux-de-Fonds: Commission Sp'el'ologie de la Socie'te' helve'tique des sciences naturelles.



- Girault, F., Adhikari, L. B., France-Lanord, C., Agrinier, P., Koirala, B. P., Bhattarai, M., Mahat, S. S., Groppo, C., Rolfo, F., Bollinger, L., & Perrier, F. (2018). Persistent CO₂ emissions and hydrothermal unrest following the 2015 earthquake in Nepal. *Nature Communications*, 9(1), 2956. <https://doi.org/10.1038/s41467-018-05138-z>
- 830
- Hasenmueller, E. A., Gu, X., Weitzman, J. N., Adams, T. S., Stinchcomb, G. E., Eissenstat, D. M., Drohan, P. J., Brantley, S. L., & Kaye, J. P. (2017). Weathering of rock to regolith: The activity of deep roots in bedrock fractures. *Geoderma*, 300, 11–31. <https://doi.org/10.1016/j.geoderma.2017.03.020>
- 835
- Hashimoto, S., & Komatsu, H. (2006). Relationships between soil CO₂ concentration and CO₂ production, temperature, water content, and gas diffusivity: Implications for field studies through sensitivity analyses. *Journal of Forest Research*, 11(1), 41–50. <https://doi.org/10.1007/s10310-005-0185-4>
- Jeannin, P.-Y. (1998). *Structure et comportement hydraulique des aquifères karstiques*, [Unpublished doctoral dissertation], University of Neuchâtel.
- 840
- Jeannin, P.-Y., Hessenauer, M., Malard, A., & Chapuis, V. (2016). Impact of global change on karst groundwater mineralization in the Jura Mountains. *Science of The Total Environment*, 541, 1208–1221. <https://doi.org/10.1016/j.scitotenv.2015.10.008>
- 845
- Kähkönen, M., Wittmann, C., Kurolo, J., Ilvesniemi, H., & Salkinoja-Salonen, M. (2001). Microbial activity of boreal forest soil in a cold climate. *Boreal Environment Research*, 6, 19–28.
- Keeling, C. D. (1961). The concentration and isotopic abundances of carbon dioxide in rural and marine air. *Geochimica et Cosmochimica Acta*, 24(3), 277–298. [https://doi.org/10.1016/0016-7037\(61\)90023-0](https://doi.org/10.1016/0016-7037(61)90023-0)
- 850
- Keller, C. K. (2019). Carbon Exports from Terrestrial Ecosystems: A Critical-Zone Framework. *Ecosystems*, 22(8), 1691–1705. <https://doi.org/10.1007/s10021-019-00375-9>
- 855
- Kokoska, S., & Zwillinger, D. (2000). *CRC Standard Probability and Statistics Tables and Formulae, Student Edition*. CRC Press.
- Kottek, M., Grieser, J., Beck, C., Rudolf, B., & Rubel, F. (2006). World Map of the Köppen-Geiger Climate Classification Updated. *Meteorologische Zeitschrift*, 15, 259–263. <https://doi.org/10.1127/0941-2948/2006/0130>
- 860



- Kukuljan, L., Gabrovšek, F., Covington, M. D., & Johnston, V. E. (2021). CO₂ dynamics and heterogeneity in a cave atmosphere: Role of ventilation patterns and airflow pathways. *Theoretical and Applied Climatology*, 146(1), 91–109. <https://doi.org/10.1007/s00704-021-03722-w>
- 865 Li, Y., Yang, Y., Wang, X., Luo, W., Zhao, J., Sun, Z., Ye, Z., Chen, X., Shi, X., Xu, Y., & Baker, J. L. (2024). Sources and transport of CO₂ in the karst system of Jiguan Cave, Funiu Mountains, China. *Science of The Total Environment*, 918, 170507. <https://doi.org/10.1016/j.scitotenv.2024.170507>
- Mattey, D. P., Atkinson, T. C., Barker, J. A., Fisher, R., Latin, J.-P., Durrell, R., & Ainsworth, M. (2016). Carbon dioxide, ground air and carbon cycling in Gibraltar karst. *Geochimica et Cosmochimica Acta*, 184, 88–113. <https://doi.org/10.1016/j.gca.2016.01.041>
- 870 McDonough, L. K., Iverach, C. P., Beckmann, S., Manefield, M., Rau, G. C., Baker, A., & Kelly, B. F. J. (2016). Spatial variability of cave-air carbon dioxide and methane concentrations and isotopic compositions in a semi-arid karst environment. *Environmental Earth Sciences*, 75(8), 700. <https://doi.org/10.1007/s12665-016-5497-5>
- 875 *MeteoSwiss*. Retrieved 26 August 2024, from <https://www.meteoswiss.admin.ch/>
- Mickler, P. J., Carlson, P., Banner, J. L., Breecker, D. O., Stern, L., & Guilfoyle, A. (2019). Quantifying carbon isotope disequilibrium during in-cave evolution of drip water along discrete flow paths. *Geochimica et Cosmochimica Acta*, 244, 182–196. <https://doi.org/10.1016/j.gca.2018.09.027>
- Milanolo, S., & Gabrovšek, F. (2015). Estimation of carbon dioxide flux degassing from percolating waters in a karst cave: Case study from Bijambare cave, Bosnia and Herzegovina. *Geochemistry*, 75(4), 465–474. <https://doi.org/10.1016/j.chemer.2015.10.004>
- 885
- Mook, W. G., Bommerson, J. C., & Staverman, W. H. (1974). Carbon isotope fractionation between dissolved bicarbonate and gaseous carbon dioxide. *Earth and Planetary Science Letters*, 22(2), 169–176. [https://doi.org/10.1016/0012-821X\(74\)90078-8](https://doi.org/10.1016/0012-821X(74)90078-8)
- 890
- Moyes, A. B., Gaines, S. J., Siegwolf, R. T. W., & Bowling, D. R. (2010). Diffusive fractionation complicates isotopic partitioning of autotrophic and heterotrophic sources of soil respiration. *Plant, Cell and Environment*, 33(11), 1804–1819. [Scopus. https://doi.org/10.1111/j.1365-3040.2010.02185.x](https://doi.org/10.1111/j.1365-3040.2010.02185.x)



- 895 Noronha, A. L., Johnson, K. R., Southon, J. R., Hu, C., Ruan, J., & McCabe-Glynn, S. (2015). Radiocarbon evidence for
decomposition of aged organic matter in the vadose zone as the main source of speleothem carbon. *Quaternary Science
Reviews*, 127, 37–47. <https://doi.org/10.1016/j.quascirev.2015.05.021>
- 900 Pataki, D. E., Ehleringer, J. R., Flanagan, L. B., Yakir, D., Bowling, D. R., Still, C. J., Buchmann, N., Kaplan, J. O., & Berry,
J. A. (2003). The application and interpretation of Keeling plots in terrestrial carbon cycle research. *Global Biogeochemical
Cycles*, 17(1). <https://doi.org/10.1029/2001GB001850>
- Perrin, J., Jeannin, P.-Y., & Zwahlen, F. (2003). Epikarst storage in a karst aquifer: A conceptual model based on isotopic data,
Milandre test site, Switzerland. *Journal of Hydrology*, 279(1), 106–124. [https://doi.org/10.1016/S0022-1694\(03\)00171-9](https://doi.org/10.1016/S0022-1694(03)00171-9)
- 905 Planavsky, N., Partin, C., & Bekker, A. (2015). *Carbon Isotopes as a Geochemical Tracer* (pp. 366–371).
https://doi.org/10.1007/978-3-662-44185-5_228
- Powers, H. H., Hunt, J. E., Hanson, D. T., & McDowell, N. G. (2010). A dynamic soil chamber system coupled with a tunable
diode laser for online measurements of $\delta^{13}\text{C}$, $\delta^{18}\text{O}$, and efflux rate of soil-respired CO_2 . *Rapid Communications in Mass
Spectrometry*, 24(3), 243–253. <https://doi.org/10.1002/rcm.4380>
- 910 Pumpanen, J., Ilvesniemi, H., PERÄMÄKi, M., & Hari, P. (2003). Seasonal patterns of soil CO_2 efflux and soil air CO_2
concentration in a Scots pine forest: Comparison of two chamber techniques. *Global Change Biology*, 9(3), 371–382.
<https://doi.org/10.1046/j.1365-2486.2003.00588.x>
- 915 Ravn, N. R., Michelsen, A., & Reboleira, A. S. P. S. (2020). Decomposition of Organic Matter in Caves. *Frontiers in Ecology
and Evolution*, 8. <https://doi.org/10.3389/fevo.2020.554651>
- Reimer, P., Brown, T., & Reimer, R. (2004). Discussion: Reporting and Calibration of Post-Bomb ^{14}C Data. *Radiocarbon*,
46, 1299–1304. <https://doi.org/10.1017/S0033822200033154>
- 920 Risk, D., Nickerson, N., Phillips, C. L., Kellman, L., & Moroni, M. (2012). Drought alters respired $\delta^{13}\text{C}\text{CO}_2$ from autotrophic,
but not heterotrophic soil respiration. *Soil Biology and Biochemistry*, 50, 26–32. <https://doi.org/10.1016/j.soilbio.2012.01.025>
- 925 Sánchez-Cañete, E. P., Barron-Gafford, G. A., & Chorover, J. (2018). A considerable fraction of soil-respired CO_2 is not
emitted directly to the atmosphere. *Scientific Reports*, 8(1), 13518. <https://doi.org/10.1038/s41598-018-29803-x>



- Savoy, L., Surbeck, H., & Hunkeler, D. (2011). Radon and CO₂ as natural tracers to investigate the recharge dynamics of karst aquifers. *Journal of Hydrology*, 406(3), 148–157. <https://doi.org/10.1016/j.jhydrol.2011.05.031>
- 930 Shi, Z., Allison, S. D., He, Y., Levine, P. A., Hoyt, A. M., Beem-Miller, J., Zhu, Q., Wieder, W. R., Trumbore, S., & Randerson, J. T. (2020). The age distribution of global soil carbon inferred from radiocarbon measurements. *Nature Geoscience*, 13(8), 555–559. <https://doi.org/10.1038/s41561-020-0596-z>
- Sommaruga, A. (2011). From the central Jura mountains to the molasse basin (France and Switzerland). *Swiss Bulletin Fuer*
935 *Angewandte Geologie*, 16(2), 63–75.
- Staddon, P. (2004). Carbon isotopes in functional soil ecology. *Trends in Ecology & Evolution*, 19, 148–154. <https://doi.org/10.1016/j.tree.2003.12.003>
- 940 Stewart, B., Zhi, W., Sadayappan, K., Sterle, G., Harpold, A., & Li, L. (2022). Soil CO₂ Controls Short-Term Variation but Climate Regulates Long-Term Mean of Riverine Inorganic Carbon. *Global Biogeochemical Cycles*, 36(8), e2022GB007351. <https://doi.org/10.1029/2022GB007351>
- Swisstopo*. Retrieved 1 December 2024, from <https://www.swisstopo.admin.ch/en>
945
- Synal, H.-A., Stocker, M., & Suter, M. (2007). MICADAS: A new compact radiocarbon AMS system. *Nuclear Instruments and Methods in Physics Research Section B: Beam Interactions with Materials and Atoms*, 259(1), 7–13. <https://doi.org/10.1016/j.nimb.2007.01.138>
- 950 Szidat, S. (2020). ¹⁴C Research at the Laboratory for the Analysis of Radiocarbon with AMS (LARA), University of Bern. *CHIMIA*, 74(12), Article 12. <https://doi.org/10.2533/chimia.2020.1010>
- Trumbore, S. (2000). Age of Soil Organic Matter and Soil Respiration: Radiocarbon Constraints on Belowground C Dynamics. *Ecological Applications*, 10(2), 399–411. [https://doi.org/10.1890/1051-0761\(2000\)010\[0399:AOSOMA\]2.0.CO;2](https://doi.org/10.1890/1051-0761(2000)010[0399:AOSOMA]2.0.CO;2)
955
- Tune, A., Druhan, J., Wang, J., Bennett, P., & Rempe, D. (2020). Carbon Dioxide Production in Bedrock Beneath Soils Substantially Contributes to Forest Carbon Cycling. *Journal of Geophysical Research: Biogeosciences*, 125. <https://doi.org/10.1029/2020JG005795>



960 Unger, S., Máguas, C., Pereira, J. S., Aires, L. M., David, T. S., & Werner, C. (2010). Disentangling drought-induced variation in ecosystem and soil respiration using stable carbon isotopes. *Oecologia*, 163(4), 1043–1057. <https://doi.org/10.1007/s00442-010-1576-6>

Van Rossum, G. & Drake, F.L., 2009. *Python 3 Reference Manual*, Scotts Valley, CA: CreateSpace.

965

Vaughn, L. J. S., & Torn, M. S. (2018). Radiocarbon measurements of ecosystem respiration and soil pore-space CO₂ in Utqiagvik (Barrow), Alaska. *Earth System Science Data*, 10(4), 1943–1957. <https://doi.org/10.5194/essd-10-1943-2018>

970 Wacker, L., Christl, M., & Synal, H.-A. (2010b). Bats: A new tool for AMS data reduction. *Nuclear Instruments and Methods in Physics Research Section B: Beam Interactions with Materials and Atoms*, 268(7), 976–979. <https://doi.org/10.1016/j.nimb.2009.10.078>

975 Wacker, L., Němec, M., & Bourquin, J. (2010a). A revolutionary graphitisation system: Fully automated, compact and simple. *Nuclear Instruments and Methods in Physics Research Section B: Beam Interactions with Materials and Atoms*, 268(7), 931–934. <https://doi.org/10.1016/j.nimb.2009.10.067>

980 Wan, J., Tokunaga, T. K., Dong, W., Williams, K. H., Kim, Y., Conrad, M. E., Bill, M., Riley, W. J., & Hubbard, S. S. (2018). Deep Unsaturated Zone Contributions to Carbon Cycling in Semiarid Environments. *Journal of Geophysical Research: Biogeosciences*, 123(9), 3045–3054. <https://doi.org/10.1029/2018JG004669>

980

Weissert, H., & Mohr, H. (1996). Late Jurassic climate and its impact on carbon cycling. *Palaeogeography, Palaeoclimatology, Palaeoecology*, 122(1), 27–43. [https://doi.org/10.1016/0031-0182\(95\)00088-7](https://doi.org/10.1016/0031-0182(95)00088-7)

985 Wingler, A., & Hennessy, D. (2016). Limitation of Grassland Productivity by Low Temperature and Seasonality of Growth. *Frontiers in Plant Science*, 7. <https://doi.org/10.3389/fpls.2016.01130>

990 Wu, J., Zhang, Q., Yang, F., lei, Y., Zhang, Q., & Cheng, X. (2017). Does short-term litter input manipulation affect soil respiration and its carbon-isotopic signature in a coniferous forest ecosystem of central China? *Applied Soil Ecology*, 113, 45–53. <https://doi.org/10.1016/j.apsoil.2017.01.013>

990

Zhang, H., Zhou, Z., Dong, H., Yan, L., Ding, S., Huang, J., Gong, X., & Su, D. (2023). Seasonal variations of cave dripwater hydrogeochemical parameters and $\delta^{13}\text{C}_{\text{DIC}}$ in the subtropical monsoon region and links to regional hydroclimate. *Science of The Total Environment*, 881, 163509. <https://doi.org/10.1016/j.scitotenv.2023.163509>